View Article Online / Journal Homepage / Table of Contents for this issue

PCCP

Physical Chemistry Chemical Physics

www.rsc.org/pccp

Volume 14 | Number 48 | 28 December 2012 | Pages 16489–16796

Published on 06 September 2012. Downloaded by Tsinghua University on 06/04/2014 04:02:06.

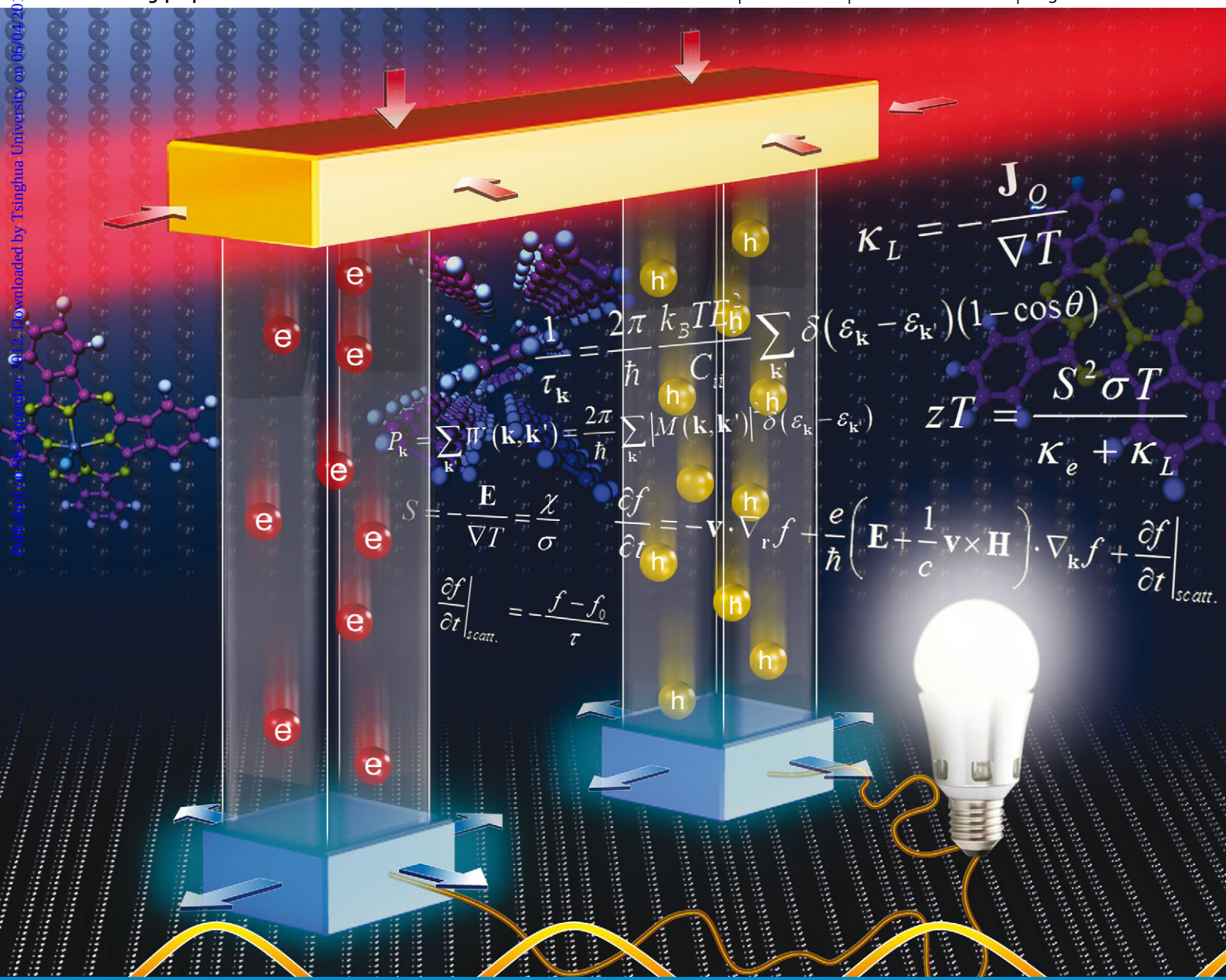

Includes a collection of articles on the theme of Computational Catalysis

ISSN 1463-9076

PERSPECTIVE
Shuai *et al.*
Modeling thermoelectric transport in organic materials

1463-9076(2012)14:48;1-I

PCCP

View Article Online
Dynamic Article Links

Cite this: *Phys. Chem. Chem. Phys.*, 2012, **14**, 16505–16520

www.rsc.org/pccp

PERSPECTIVE

Modeling thermoelectric transport in organic materials

Dong Wang,[a] Wen Shi,[a] Jianming Chen,[b] Jinyang Xi[a] and Zhigang Shuai*[ab]

Received 3rd August 2012, Accepted 6th September 2012
DOI: 10.1039/c2cp42710a

Thermoelectric energy converters can directly convert heat to electricity using semiconducting materials *via* the Seebeck effect and electricity to heat *via* the Peltier effect. Their efficiency depends on the dimensionless thermoelectric figure of merit of the material, which is defined as $zT = S^2\sigma T/\kappa$ with S, σ, κ, and T being the Seebeck coefficient, electrical conductivity, thermal conductivity, and absolute temperature respectively. Organic materials for thermoelectric applications have attracted great attention. In this review, we present our recent progress made in developing theories and computational schemes to predict the thermoelectric figure of merit at the first-principles level. The methods have been applied to model thermoelectric transport in closely-packed molecular crystals and one-dimensional conducting polymer chains. The physical insight gained in these studies will help in the design of efficient organic thermoelectric materials.

1 Introduction

The thermoelectric power generators and coolers interconvert heat and electricity *via* the Seebeck and the Peltier effect. If a temperature difference is applied to a material, a voltage difference is created under open circuit conditions. The phenomenon is known as the Seebeck effect. The Seebeck coefficient S, aka the thermopower, is defined as the ratio of the voltage difference to the temperature difference. For p-type semiconductors the Seebeck coefficient is positive, and for n-type semiconductors it is negative. If an electrical current is imposed on a thermocouple composed of different materials, heat is generated at one junction and absorbed at the other, which is known as the Peltier effect. The Peltier coefficient Π is defined as the ratio of the rate of heat exchange to the electrical current. The thermoelectric coefficients obey the Kelvin relationships $\Pi = ST$.[1] Thermoelectric cooling and power generation require joining two different materials, usually a p-type semiconductor with a positive S and an n-type semiconductor with a negative S. Therefore, it is Π and S of couples that matter in practice. Two irreversible processes, thermal conduction and Joule heating, lower the performance

[a] *MOE Key Laboratory of Organic OptoElectronics and Molecular Engineering, Department of Chemistry, Tsinghua University, Beijing 100084, P. R. China. E-mail: dong913@tsinghua.edu.cn; Tel: +86 1062772969*
[b] *Key Laboratory of Organic Solids, Beijing National Laboratory for Molecular Sciences (BNLMS), Institute of Chemistry, Chinese Academy of Sciences, Beijing 100190, P. R. China. E-mail: zgshuai@iccas.ac.cn; Fax: +86 10 62525573; Tel: +86 10 62797689*

Dong Wang

Dong Wang received her PhD in physical chemistry supervised by Prof. Qingshi Zhu at the University of Science and Technology of China in 2000. She then worked as a postdoctoral researcher with Prof. Eitan Geva at the University of Michigan, USA, and with Prof. Gregory Voth at the University of Utah, USA. Since 2009, she became an associate professor in the Department of Chemistry, Tsinghua University. Her research interests include the theoretical characterization of thermoelectric transport in organic materials and computer simulations of self-assembly in soft matter.

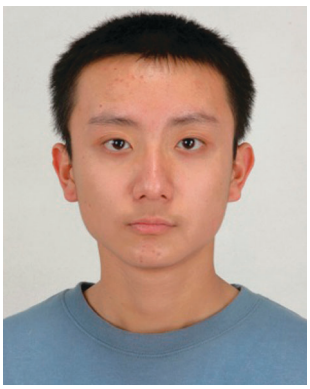

Wen Shi

Wen Shi graduated with a BS degree majoring in applied chemistry from China Agricultural University, Beijing, China in 2012 and is presently a PhD student in Prof. Zhigang Shuai's group at Tsinghua University. His research interests are theoretical modeling of thermoelectric transport in organic materials.

Published on 06 September 2012. Downloaded by Tsinghua University on 06/04/2014 04:02:06.

View Article Online

Published on 06 September 2012. Downloaded by Tsinghua University on 06/04/2014 04:02:06.

of thermoelectric devices to less than the thermodynamic limit. A good thermoelectric material must combine a large Seebeck coefficient S with high electrical conductivity σ and low thermal conductivity κ. In the most simplified cases, assuming that S, σ, and κ do not vary with temperature, the maximum efficiency of a thermoelectric device can be computed analytically, and the resulting efficiency is given by[2,3]

$$\eta = \frac{\Delta T}{T_h} \times \frac{\sqrt{1+Z\bar{T}}-1}{\sqrt{1+Z\bar{T}}+T_c/T_h}, \quad (1)$$

where T_h is the temperature at the hot and T_c at the cold junction, $\Delta T = T_h - T_c$, and $\bar{T} = (T_h + T_c)/2$. The thermoelectric figure of merit is defined as

$$Z = \frac{(S_p - S_n)^2}{[(\kappa_p/\sigma_p)^{1/2} + (\kappa_n/\sigma_n)^{1/2}]^2}, \quad (2)$$

where the subscripts p and n denote properties related to the p-type and n-type semiconducting thermoelectric materials. If there were no irreversible effects, the efficiency is $\Delta T/T_h$, the Carnot limit of heat engines. If the thermoelectric properties of the p-type and n-type materials are similar, Z for a thermocouple is approximately the average of z for individual materials, and it is practical to optimize the materials separately. The dimensionless figure of merit of a material is defined as $zT = S^2\sigma T/\kappa$. It is an intensive material property of prime importance. Both electrons and phonons are heat carriers, so the thermal conductivity has two contributions, the electrical thermal conductivity κ_e and the lattice thermal conductivity κ_L. An efficient thermoelectric material should combine properties such as large Seebeck coefficient, high electrical conductivity, and low thermal conductivity. In other words, in the design of thermoelectric materials phonon transport should be suppressed and at the same time electrical transport should be enhanced. These requirements are very often conflicting, which poses a huge challenge to optimization of thermoelectric materials.

In recent years, there have been significant advances in the field of thermoelectric materials and devices. In addition to developing the next generation of thermoelectric materials, it has been recognized that nanostructures and low-dimensional structures are able to improve the thermoelectric performance of bulk materials. By introducing nanoscale constituents in host materials and increasing interfaces, the power factor $S^2\sigma$ can be enhanced and the thermal conductivity reduced. To find out significant progress made in the field of thermoelectrics during the past years, we refer our readers to recent reviews that cover different aspects of the field.[4–7] In this perspective, we show specific interest in organic thermoelectric materials. The best bulk thermoelectric materials are bismuth telluride based alloys with zT around one. However, the production of the alloys is not economic nor it is environmental friendly due to the fact that these materials are toxic and Te is one of the rarest elements on earth. Compared to traditional inorganic thermoelectric materials, organic electronic materials have the advantages of being flexible, low-cost, and solution processable. Since organic materials are characterized by poor thermal conductivity, they have been suggested

Jianming Chen

Jianming Chen is currently a PhD candidate in the group of Prof. Zhigang Shuai at the Institute of Chemistry, Chinese Academy of Sciences. He obtained his BS degree at the South China University of Technology in 2007. His research interests are the first-principles calculations of thermoelectric properties in organic materials and molecular-scale simulation of self-assembly in organic electronic devices.

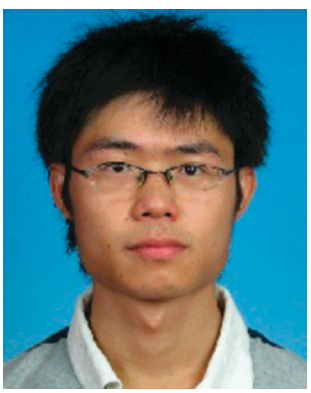

Jinyang Xi

Jinyang Xi graduated with a BS degree majoring in physics from Northeast Normal University, Changchun, China in 2009 and is presently a PhD student in Prof. Zhigang Shuai's group at Tsinghua University. His research interests are theoretical evaluation of electron–phonon scatterings and charge transport in nanomaterials and molecular crystals.

Zhigang Shuai

Zhigang Shuai, PhD 1989 Fudan University, Shanghai. 1990–2001, postdoc and research associate with Prof. Jean-Luc Brédas at the University of Mons, Belgium. 2002–2008, "Hundred-Talent" professor at the Institute of Chemistry of the Chinese Academy of Sciences in Beijing. 2008 to date, Changjiang Scholar Chair professor, Tsinghua University, Beijing. His research interests are theoretical modeling of the organic functional materials for the opto-electronic properties. 240 publications with h-index = 40. He received the Outstanding Young Investigator's Fund (2004) and Chinese Chemical Society-AkzoNobel Chemical Sciences Award (2012). He is a member of the International Academy of Quantum Molecular Science, the Academia Europaea, and a Fellow of the Royal Society of Chemistry.

 This journal is © the Owner Societies 2012

View Article Online

Published on 06 September 2012. Downloaded by Tsinghua University on 06/04/2014 04:02:06.

for thermoelectric applications. A number of conjugated polymers have been studied, such as polyacetylene, polypyrroles, polyanalines, polythiophenes, polycarbazoles, and so on, see a recent review (ref. 8). However, the best thermoelectric efficiency so far reported is 0.25, obtained in poly(3,4-ethylenedioxythiophene) (PEDOT) nanowires by the accurate control of the doping level.[9] As observed in inorganic materials, thermoelectric power factors were enhanced in PEDOT nanowires compared to those in thin films.[10] In addition to conducting polymers, small organic molecules such as pentacene have been studied for thermoelectric applications. The maximum power factor of 2×10^{-5} W m^{-1} K^{-2} was reported in the iodine doped pentacene thin film,[11] one order of magnitude higher than that in the pentacene thin film doped with 2,3,5,6-tetrafluoro-7,7,8,8-tetracyanoquinodimethane.[12] The problem associated with organic thermoelectirc materials is that the efficiency is still very low. It is known that thermoelectric power generators can become competitive with other renewable technologies provided one can develop materials with $zT > 1.5$ at the appropriate temperatures, but progress in zT values is slow. However for practical applications, it is the electricity cost that matters not the thermoelectric efficiency. There are many free heat sources in the real world, such as vehicle waste heat, even a modest fraction of this thermal waste can be recovered, the savings in fuel and reductions in carbon dioxide are considerable.

The progress made in searching for organic thermoelectric materials also raises questions on the fundamental understanding of charge and phonon transport in organic materials. Theoretical modeling of charge and phonon transport is no doubt necessary in order to develop design strategies of efficient organic thermoelectric materials. Recently, we investigated thermoelectric transport in organic molecular crystals by characterizing both electrical and phonon transport at the first-principles level.[13,14] In this review, we summarize our progress made in developing a computational scheme, which is completely parameter free, to predict thermoelectric performance of highly-ordered organic model systems. In the first part of the review, we present the theory and methodologies used to model charge carrier transport and phonon transport, which include Boltzmann transport theory, deformation potential (DP) theory, and nonequilibrium molecular dynamics (MD) method. In the second part, we show applications of the theories to molecular crystals including pentacene, rubrene, and phthalocyanines, as well as single polymer chain P3HT. The doping effect on the electrical transport coefficients, and the anisotropy and defect effects in phonon transport have been addressed. Finally, we discuss limitations of our methodologies and challenges for theoretical modeling of thermoelectric transport in organic materials.

2 Modeling thermoelectric transport at the first-principles level

The theories described below assume that electrons are delocalized in highly-ordered and closely packed conjugated systems, where doping concentration is not so high that the electron–electron correlation effect can be ignored.

2.1 Boltzmann transport theory

In the single particle approximation, the state of electrons in solids is described by a distribution function in the phase space ($\mathbf{r}$, $\mathbf{k}$) as a function of time. The electron distribution under the equilibrium follows the Fermi–Dirac distribution

$$f_0(\varepsilon_k) = \frac{1}{\exp[(\varepsilon_k - \mu)/k_B T] + 1}. \quad (3)$$

It undergoes deformation in the external fields, such as in the electric field, the electrons are accelerated causing a drift of the distribution in the $\mathbf{k}$ space. During the movement, charge carriers are subject to scatterings from the phonons and defects. The scatterings help the electrons to be restored to the equilibrium distribution. The time evolution of charge carrier distribution function in the external fields, including the electric or magnetic fields and thermal gradient, is described by the Boltzmann transport equation[15,16]

$$\frac{\partial f}{\partial t} = -\mathbf{v} \cdot \nabla_{\mathbf{r}} f + \frac{e}{\hbar}\left(\mathbf{E} + \frac{1}{c}\mathbf{v} \times \mathbf{H}\right) \cdot \nabla_{\mathbf{k}} f + \left.\frac{\partial f}{\partial t}\right|_{\text{scatt.}} \quad (4)$$

where $\mathbf{v}$ is the group velocity defined as

$$\mathbf{v} = \frac{1}{\hbar}\nabla_{\mathbf{k}} \varepsilon_{\mathbf{k}}. \quad (5)$$

To solve the equation, we invoke the relaxation time approximation for the scattering term

$$\left.\frac{\partial f}{\partial t}\right|_{\text{scatt.}} = -\frac{f - f_0}{\tau} \quad (6)$$

The relaxation time measures how quickly the electrons are restored to the equilibrium distribution *via* scatterings. In the existence of an electric field and retaining only the first-order term, the steady-state distribution is

$$f_{\mathbf{k}} = f_0(\varepsilon_{\mathbf{k}}) + e\frac{\partial f_0}{\partial \varepsilon}\tau_{\mathbf{k}}\mathbf{v}_{\mathbf{k}} \cdot \mathbf{E} \quad (7)$$

The electrical current is defined as

$$\mathbf{J} = -e\sum_{\mathbf{k}} f_{\mathbf{k}}\mathbf{v}_{\mathbf{k}} \quad (8)$$

where e is the elementary charge. Substituting eqn (7) into eqn (8) and based on Ohm's law, we obtain the expression for the electrical conductivity tensor

$$\sigma = e^2 \sum_{\mathbf{k}} \left(-\frac{\partial f_0}{\partial \varepsilon}\right)\mathbf{v}_{\mathbf{k}}\mathbf{v}_{\mathbf{k}}\tau_{\mathbf{k}} \quad (9)$$

In the derivation above, we have taken advantage of the fact that there is zero net current flow in the absence of fields.

Similarly, if a thermal gradient is applied, charge carriers diffuse, resulting in an electric field that opposes the diffusion. The net electrical current is

$$\mathbf{J} = \sigma\mathbf{E} + \chi\nabla T \quad (10)$$

The Seebeck coefficient is defined as the ratio of the electric field to the temperature gradient when the electrical

View Article Online

Published on 06 September 2012. Downloaded by Tsinghua University on 06/04/2014 04:02:06.

current is zero. We have

$$S = -\frac{\mathbf{E}}{\nabla T} = \frac{\chi}{\sigma} \tag{11}$$

The steady-state distribution function can be written as

$$\begin{aligned} f_{\mathbf{k}} &= f_0(\varepsilon_{\mathbf{k}}) + \frac{\partial f_0}{\partial \varepsilon}\frac{\varepsilon_{\mathbf{k}} - \mu}{T}\tau_{\mathbf{k}}\mathbf{v}_{\mathbf{k}} \cdot \nabla T \\ &\quad + e\frac{\partial f_0}{\partial \varepsilon}\tau_{\mathbf{k}} v_{\mathbf{k}} \cdot \mathbf{E} \end{aligned} \tag{12}$$

utilizing the relation $\frac{\partial f_0}{\partial T} = \left(-\frac{\partial f_0}{\partial \varepsilon}\right)\frac{\varepsilon-\mu}{T}$.

Substituting eqn (12) into eqn (8) and combining eqn (10), we have

$$\chi = e\sum_{\mathbf{k}}\left(-\frac{\partial f_0}{\partial \varepsilon}\right)\frac{\varepsilon_{\mathbf{k}} - \mu}{T}\mathbf{v}_{\mathbf{k}}\mathbf{v}_{\mathbf{k}}\tau_{\mathbf{k}} \tag{13}$$

The thermal gradient induces not only electrical current but also heat current, as electrons carry charges as well as energy. The heat current is defined as

$$\mathbf{J}_Q = \mathbf{J}_{\mathrm{E}} - \mu\mathbf{J}_{\mathrm{P}} \tag{14}$$

where $\mathbf{J}_{\mathrm{E}}$ is the energy current and $\mathbf{J}_{\mathrm{P}}$ is the particle current.

The heat current of charge carriers is further expressed as

$$\begin{aligned} J_Q &= \sum_{\mathbf{k}} f_{\mathbf{k}} v_{\mathbf{k}} \varepsilon_{\mathbf{k}} - \mu\sum_{\mathbf{k}} f_{\mathbf{k}}\mathbf{v}_{\mathbf{k}} \\ &= \sum_{\mathbf{k}} (\varepsilon_{\mathbf{k}} - \mu) f_{\mathbf{k}}\mathbf{v}_{\mathbf{k}} \end{aligned} \tag{15}$$

Substituting eqn (12) into eqn (15), the heat current is written as

$$\mathbf{J}_Q = -\kappa_0\nabla T - \chi T\mathbf{E} \tag{16}$$

with

$$\kappa_0 = \sum_{\mathbf{k}}\left(-\frac{\partial f_0}{\partial \varepsilon}\right)\frac{(\varepsilon_{\mathbf{k}} - \mu)^2}{T}\mathbf{v}_{\mathbf{k}}\mathbf{v}_{\mathbf{k}}\tau_{\mathbf{k}} \tag{17}$$

The electronic contribution to the thermal conductivity is defined as the ratio of the heat current to the temperature gradient when the electrical current is zero. In accordance with this definition, and in combination with eqn (11) and (16), we can identify

$$\kappa_{\mathrm{e}} = \kappa_0 - S^2\sigma T \tag{18}$$

This shows that all transport coefficients can be obtained once a kernel tensor as

$$\sum_{\mathbf{k}} \mathbf{v}_{\mathbf{k}}\mathbf{v}_{\mathbf{k}}\tau_{\mathbf{k}} \tag{19}$$

is calculated. The kernel is called the transport distribution function. The group velocity and band energy can be determined from first-principles band structure calculations. It is noted that the energy derivative of the Fermi–Dirac distribution function shows up in the expressions derived for transport coefficients. The effect of the term is that only bands close to the Fermi level contribute to electrical transport. The charge carrier concentration is defined as

$$N_n = 2\int_{CB} g(\varepsilon) f_0 d\varepsilon \tag{20}$$

for electrons and

$$N_p = 2\int_{VB} g(\varepsilon)(1 - f_0) d\varepsilon \tag{21}$$

for holes with $g(\varepsilon)$ the density of states (DOS).

We assume that band structures do not change with the Fermi level; in the rigid band approximation, doping effect is modeled simply by shifting the Fermi level position. To calculate electrical transport coefficients, the key is to determine the electron (hole) relaxation time. The scattering term can be expressed as

$$\left.\frac{\partial f}{\partial t}\right|_{\mathrm{scatt.}} = \sum_{\mathbf{k}'}\begin{bmatrix} W(\mathbf{k}', \mathbf{k}) f_{\mathbf{k}'}(1 - f_{\mathbf{k}}) \\ -W(\mathbf{k}, \mathbf{k}') f_{\mathbf{k}}(1 - f_{\mathbf{k}'}) \end{bmatrix} \tag{22}$$

where $W(\mathbf{k}, \mathbf{k}')$ is the transition probability. For elastic scatterings $\varepsilon_{\mathbf{k}'} = \varepsilon_{\mathbf{k}}$, we have $W(\mathbf{k}', \mathbf{k}) = W(\mathbf{k}, \mathbf{k}')$ and eqn (20) is simplified as

$$\left.\frac{\partial f}{\partial t}\right|_{\mathrm{scatt.}} = \sum_{\mathbf{k}'} W(\mathbf{k}, \mathbf{k}')(f_{\mathbf{k}'} - f_{\mathbf{k}}) \tag{23}$$

Combining eqn (6), (7), and (23), the relaxation time is expressed as

$$\frac{1}{\tau_{\mathrm{k}}} = \sum_{\mathrm{k}'} W(\mathbf{k}, \mathbf{k}')\left(1 - \frac{\mathbf{v}_{\mathbf{k}'}\tau_{\mathbf{k}'} \cdot \mathbf{e}_{\mathbf{E}}}{\mathbf{v}_{\mathbf{k}}\tau_{\mathbf{k}} \cdot \mathbf{e}_{\mathbf{E}}}\right) \tag{24}$$

where $\mathbf{e}_{\mathbf{E}}$ is the unit vector in the direction of the electric field. In principle, eqn (24) can be solved iteratively. To avoid complexity, eqn (24) is further approximated as

$$\frac{1}{\tau_{\mathbf{k}}} = \sum_{\mathbf{k}'} W(\mathbf{k}, \mathbf{k}')(1 - \cos\theta) \tag{25}$$

where $(1 - \cos\theta)$ describes the scattering angle weighting factor for a spherical energy surface. θ is the angle between the two wave vectors. By applying the Fermi's Golden rule, the scattering probability can be written as

$$P_{\mathbf{k}} = \sum_{\mathbf{k}'} W(\mathbf{k}, \mathbf{k}') = \frac{2\pi}{\hbar}\sum_{\mathbf{k}'} |M(\mathbf{k}, \mathbf{k}')|^2 \delta(\varepsilon_{\mathbf{k}} - \varepsilon_{\mathbf{k}'}) \tag{26}$$

where $|M(\mathbf{k},\mathbf{k}')|^2$ is the scattering matrix element. Comparing eqn (25) and (26), we find that the relaxation time is different from the free collision time of charge carriers by a weighting factor. Scatterings of different angles contribute differently to the transport coefficients. Now, the difficulty is to calculate the scattering matrix element. Here we only consider the dominant scattering of a thermal electron or hole by acoustic phonons within the DP theory.

2.2 Deformation potential theory

The DP theory was proposed by Bardeen and Shockley[17] in the 1950s to describe the charge transport in nonpolar semiconductors. It is based on the assumption that local deformations produced by the lattice waves are similar to

 This journal is © the Owner Societies 2012

View Article Online

Published on 06 September 2012. Downloaded by Tsinghua University on 06/04/2014 04:02:06.

those in homogeneously deformed crystals. Actually in the long wavelength limit, the acoustic lattice waves are equivalent to the elastic waves if viewing crystals as continuous media. Accordingly effective potentials produced by acoustic waves of long wavelength are called deformation potentials. Since the acoustic phonon energy in the long wavelength limit is negligible compared to the electronic energy, the scatterings are elastic. Deformation potentials, which are defined as $\Delta V = E_1\Delta$ with E_1 being the DP constant and Δ the lattice dilation, can produce perturbations to electrons in the periodic potential of a crystal lattice. It is noted that only longitudinal waves contribute to the deformation. The displacement of an atom at site $\mathbf{R}_n$ resulting from a longitudinal lattice wave of wave vector $\mathbf{q}$ is

$$\mathbf{u}(\mathbf{R}_n) = \frac{1}{\sqrt{N}}\mathbf{e}_\mathbf{q}[a_\mathbf{q}\exp(i\mathbf{q}\cdot\mathbf{R}_n) + a_\mathbf{q}^*\exp(-i\mathbf{q}\cdot\mathbf{R}_n)] \quad (27)$$

where N is the number of lattice sites in the unit volume, and $\mathbf{e}_\mathbf{q}$ and $a_\mathbf{q}$ are the unit vectors of $\mathbf{q}$ and amplitude of the lattice wave. In the long wavelength limit, the dilation resulting from the elastic wave is

$$\Delta(\mathbf{r}) = \frac{\partial\mathbf{u}(\mathbf{r})}{\partial\mathbf{r}} = \frac{i}{\sqrt{N}}q\begin{bmatrix} a_\mathbf{q}\exp(i\mathbf{q}\cdot\mathbf{r}) \\ -a_\mathbf{q}^*\exp(-i\mathbf{q}\cdot\mathbf{r}) \end{bmatrix} \quad (28)$$

The matrix element for electrons to be scattered from the Bloch state $|\mathbf{k}\rangle$ to $|\mathbf{k}'\rangle$ is

$$|M(\mathbf{k},\mathbf{k}')|^2 = |\langle\mathbf{k}|\Delta V|\mathbf{k}'\rangle|^2 = \frac{1}{N}{E_1}^2q^2|a_\mathbf{q}|^2 \quad (29)$$

with $\mathbf{q} = \pm(\mathbf{k}' - \mathbf{k})$ being the selection rule. At high temperatures, the lattice wave is fully excited, the amplitude of the wave is given by $|a_\mathbf{q}|^2 = k_\mathrm{B}/2mq^2v_\mathrm{a}^2$ according to the equipartition theorem, where m is the mass per lattice site, and v_a is the velocity of the acoustic wave. The thermal averaged scattering matrix element becomes

$$|M(\mathbf{k},\mathbf{k}')|^2 = \frac{k_\mathrm{B}T{E_1}^2}{C_{ii}} \quad (30)$$

where $C_{ii} = \rho v_a^2 = Nmv_a^2$ is the elastic constant for longitudinal strain in the direction of the wave vector $\mathbf{q}$.

Combining eqn (25), (26), and (30) and assuming that the scattering matrix element is independent of the direction of wave propagation, the relaxation time due to scatterings from longitudinal acoustic phonons in the deformation potential approximation can be expressed as[18]

$$\frac{1}{\tau_\mathbf{k}} = \frac{2\pi}{\hbar}\frac{k_\mathrm{B}T{E_1}^2}{C_{ii}}\sum_{\mathbf{k}'}\delta(\varepsilon_\mathbf{k} - \varepsilon_{\mathbf{k}'})(1-\cos\theta) \quad (31)$$

The deformation potential constant for electrons is calculated as the conduction band energy shift upon dilation, that for holes is calculated as the valence band energy shift upon dilation. The elastic constant is calculated as the second-order derivative of total energy with respect to dilation. The lattice is usually deformed individually in three crystal directions, and the scattering matrix element in each crystal direction is calculated and subsequently averaged. The relaxation time and all electrical transport coefficients are obtained once band structures, the deformation potential constant and elastic constant are determined. It is noted that electrons in real crystals are subject to scatterings by acoustic phonons, optical phonons, defects or impurities, the total relaxation time can be described by Matthiessen's rule

$$\frac{1}{\tau} = \frac{1}{\tau_\mathrm{ac}} + \frac{1}{\tau_\mathrm{op}} + \frac{1}{\tau_\mathrm{imp}} + \ldots \quad (32)$$

The dominant scattering mechanism in a perfect crystal arises from electron–phonon couplings. At present, accurate determination of the relaxation time still poses a challenging task.

2.3 Molecular dynamics simulations of phonon transport

Both electrons and phonons contribute to thermal transport. For not-so-heavily-doped semiconductors, the lattice thermal conductivity usually dominates over the electronic contribution. Modeling phonon transport constitutes a crucial step in theoretical characterization of thermoelectric transport. In real materials phonons are scattered by other phonons, defects, impurities, and boundaries, which gives rise to finite lifetimes or mean free paths of phonons and in turn finite lattice thermal conductivities. In perfect crystals, phonon–phonon interactions arising from anharmonic lattice vibrations are the only scattering mechanism that contributes to phonon transport.

The methods that can be used to calculate lattice thermal conductivity fall mainly into two categories. One class of approaches is based on kinetic theories like Boltzmann transport theroy.[19] In applying Boltzmann transport equation (BTE) to extracting lattice thermal conductivities, one needs to get such parameters as phonon dispersion relations, phonon density of states, and phonon relaxation times. However as we have seen in modeling charge transport, it is challenging to obtain relaxation times because various scattering mechanisms have to be included explicitly. Alternatively, molecular dynamics simulations represent another class of approaches by which lattice thermal conductivities can be derived directly. Besides, parameters required by the BTE, such as phonon dispersion relations and phonon density of states can be easily obtained from MD simulations. Given accurate classical force fields developed to describe interactions between atoms, employing MD simulations to extract lattice thermal conductivities is straightforward.

Both equilibrium and nonequilibrium MD approaches have been extensively used to extract lattice thermal conductivities.[20–23] The equilibrium MD method is based on the Green–Kubo formalism derived from the linear response theory, in which the thermal conductivity is expressed in terms of heat current correlation functions.[24] However, expressions for heat current are quite complicated for molecular systems where many-body interactions are present, which has limited applications of equilibrium MD approach to simple systems described by pair-wise or three-body potentials. In our study organic materials including molecular crystals and conducting polymers are of interest, so the nonequilibrium MD method is applicable. In the nonequilibrium MD approach, a heat flux across the system is generated, and the resulting temperature gradient is measured after the system has established a steady state.

View Article Online

Published on 06 September 2012. Downloaded by Tsinghua University on 06/04/2014 04:02:06.

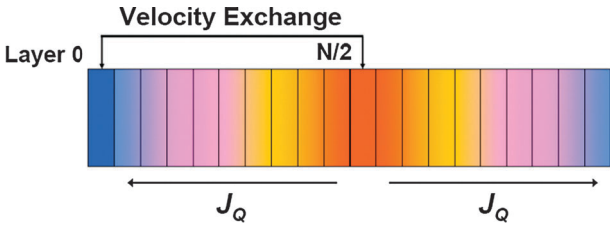

Fig. 1 Schematic representation of the simulation box and the velocity exchange algorithm of Müller–Plathe used for nonequilibrium MD simultaions. Reprinted with permission from ref. 14. Copyright 2011 American Chemical Society.

The lattice thermal conductivity is subsequently calculated according to the Fourier's law

$$\kappa_{\mathrm{L}} = -\frac{\mathbf{J}_Q}{\nabla T}. \tag{33}$$

Different algorithms have been proposed to generate the heat flux, including the velocity rescaling method of Jund and Jullien,[25] Ikeshoji and Hafskjold,[26] and the velocity exchange method of Müller-Plathe and Reith.[27] The Müller-Plathe algorithm[27,28] was adopted in our study.[14] The idea of the algorithm is to exchange velocities between two particles with the same mass in different regions of the simulations box. The unphysical exchange of velocities produces a heat flux, which in turn induces a temperature gradient in the system. In the nonequilibrium MD simulations of molecular crystals, the unit cell was first replicated in three crystal directions **a**, **b**, and **c** to build up a supercell. The supercell, which constituted the simulation box, was elongated in the direction of heat propagation. As an illustration, a simulation box that is elongated in the direction of lattice vector **a** is shown in Fig. 1. Periodic boundary conditions were applied in all three dimensions. The simulation box was then divided into N layers along the **a** axis, labeled as layer 0, 1, ..., $N-1$, respectively, from left to right. If the simulation box is triclinic, the division has to be done parallel to the box faces whose normal is in the direction of **a***, so the heat propagates in the direction of **a***, not **a**. During the exchange of velocities, the hottest carbon atom in the far left layer, layer 0, and the coldest carbon atom in the middle layer, layer $N/2$ were selected. The velocity swapping was performed at every 500 or 1000 steps in our simulations. Over time, this induced a temperature gradient in the system. The temperature of layer 0, which acted as a heat sink, decreased whereas that of layer $N/2$, which acted as heat source, increased. The heat flux imposed was calculated by the energy transferred per time and area

$$J_Q = \frac{1}{2At}\sum_{\text{transfers}} (\tfrac{1}{2}mv_{\text{hot}}^2 - \tfrac{1}{2}mv_{\text{cold}}^2) \tag{34}$$

where A is the cross sectional area, m is the mass of carbon atom, t is the length of simulation. Under periodic boundary conditions, energy flows in opposite directions, so the energy transferred should be divided by two in the above equation. After a steady state was established, the local temperature of each layer was calculated from the time average of kinetic energies of the particles in that layer.

An issue concerned with the nonequilibrium MD approach is that the thermal conductivity depends strongly on the box length in the direction of heat propagation. This size effect, arising from phonon scatterings at the boundaries of the simulation box, is usually non-negligible and can only be corrected by the extrapolation procedure.[22,29] According to the kinetic theory of thermal conduction, the thermal conductivity of an isotropic system can be expressed as

$$\kappa_{\mathrm{L}} = \frac{1}{3}\frac{C_v}{V}vl = \frac{1}{3}\rho c_v v^2 \tau. \tag{35}$$

where C_v and c_v are the constant-volume and specific heat capacities respectively, V is the volume, ρ is the mass density, τ is the phonon relaxation time, and v and l are the effective phonon velocity and mean free path respectively. If assuming that phonon scatterings at the box boundaries act independently of scatterings in the true bulk crystal, the phonon relaxation time from the MD simulations can be decomposed into[29]

$$\tau_{\mathrm{MD}}^{-1} = \tau_{\mathrm{bulk}}^{-1} + \tau_{\mathrm{box}}^{-1} \tag{36}$$

where $\tau_{\mathrm{box}}^{-1} = \frac{v}{L/2}$ and L is the box length. The lattice thermal conductivity obtained from MD simulations is then related to the size of the simulation box by[22,29]

$$\frac{1}{\kappa_{\mathrm{MD}}} = \frac{3}{\rho c_v v^2}\tau_{\mathrm{MD}}^{-1} = \frac{3}{\rho c_v v^2}(\tau_{\mathrm{bulk}}^{-1} + \frac{2v}{L}) \equiv A + \frac{B}{L}. \tag{37}$$

We performed nonequilibrium MD simulations with several box lengths, and extracted the lattice thermal conductivity of true bulk crystal by extrapolation *via* eqn (37).

3 Thermoelectric transport in molecular crystals

3.1 Pentacene and rubrene

The Seebeck coefficient in thin films of pentacene and single crystals of rubrene has been successfully measured using field-effect devices at temperatures between 295 K and 200 K.[30] It was found that the Seebeck coefficient falls in the range of 0.3–1 mV K^{-1}, and decreases logarithmically with increasing gate voltage. Thermal transport measurements showed that room-temperature thermal conductivities of pentacene thin films and rubrene single crystals were on the order of 0.5 W m^{-1} K^{-1}.[31,32] The large Seebeck coefficients and low thermal conductivities indicate that pentacene and rubrene could be potentially good thermoelectric materials.

As a demonstration of the theories introduced above, we investigate thermoelectric transport in pentacene and rubrene crystals by a combination of first-principles band structure calculations and Boltzmann transport theroy in the constant relaxation time approximation. The relaxation time is taken as a constant parameter which is derived from the experimental mobility data. We start from band structure calculations based on crystal structures of pentacene and rubrene.

3.1.1 Band structures. Pentacene is known to form different crystal structures under different conditions. In our study, the crystal structure of the pentacene film grown on SiO_2 is adopted.[33] Rubrene crystal has an orthorhombic structure.[34] In pentacene and rubrene crystals, an in-plane herringbone

 This journal is © the Owner Societies 2012

View Article Online

Published on 06 September 2012. Downloaded by Tsinghua University on 06/04/2014 04:02:06.

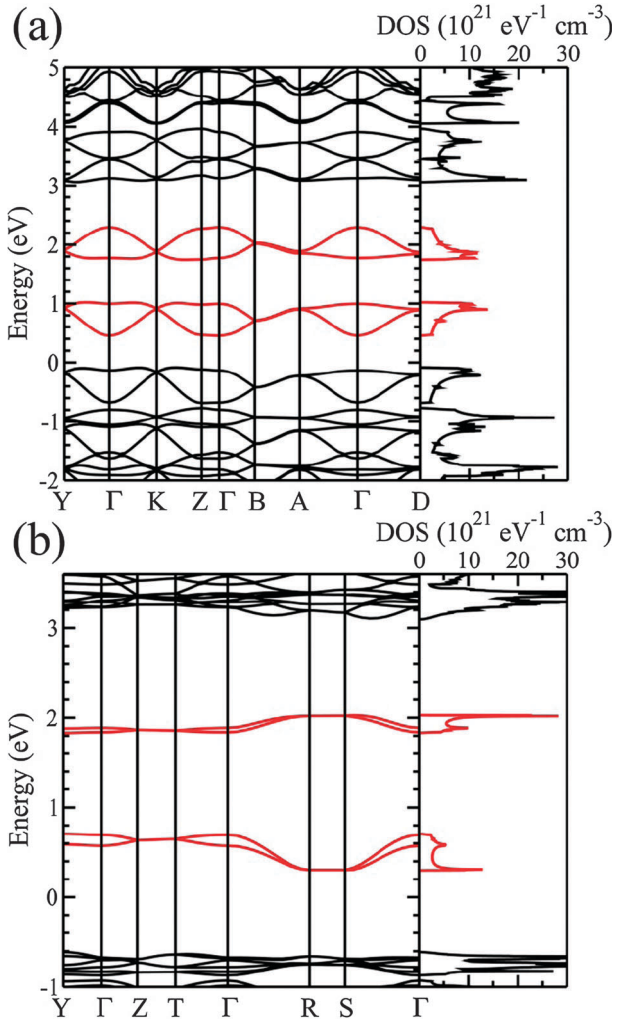

Fig. 2 Band structures and DOS of (a) pentacene and (b) rubrene. The reciprocal coordinates of high-symmetry points are Γ = (0, 0, 0), Y = (0.5, 0, 0), B = (0, 0.5, 0), Z = (0, 0, 0.5), A = (0.5, 0.5, 0), D = (0.5, 0.5, −0.5), and K = (0.5, 0, 0.5), respectively, in pentacene and Γ = (0, 0, 0), Y = (0.5, 0.5, 0), Z = (0, 0, 0.5), T = (0.5, 0.5, 0.5), R = (0, 0.5, 0.5), and S = (0, 0.5, 0), respectively, in rubrene. Reprinted with permission from ref. 13. Copyright 2009 American Institute of Physics.

arrangement of two inequivalent molecules and a layered structure in the perpendicular direction are found. The first-principles band structure calculations are performed by the projector-augmented wave method (PAW)[35,36] with the Perdew–Burke–Ernzerhof (PBE) generalized gradient approximation (GGA)[37] as implemented in Vienna *ab initio* simulation package (VASP).[38] The atomic coordinates are optimized on a 6 × 6 × 4 and 4 × 4 × 4 Monkhorst–Pack **k**-mesh[39] respectively for pentacene and rubrene.

The band structures and density of states are depicted in Fig. 2. There are two inequivalent molecules in a unit cell of pentacene and rubrene, so each band in band structures appears in pair. Band dispersions of the two subbands of the highest valence band (VB) for pentacene are 468 and 306 meV, and those of the lowest conduction band (CB) are 274 and 426 meV. The values for rubrene are 345 and 403 meV for VB, 190 and 168 meV for CB. The hole transport behavior is governed by structural features of the highest VB, and electron transport is governed by that of the lowest CB. Large bandwidth is usually a characteristic feature of high mobility. A dispersed lower subband and a relatively flat upper subband are noted in the highest VB of pentacene. In contrast, band splitting in the highest VB of rubrene is quite small. Consequently, DOS of pentacene exhibits a sharp peak at the top of VB whereas DOS distribution in rubrene is relatively smooth at the top of VB. The Seebeck coefficient is determined by DOS distribution at the Fermi level, sharper distributions usually represent larger Seebeck coefficients. The calculated band gap is 0.72 eV for pentacene and 1.12 eV for rubrene. DFT calculations are known to underestimate band gaps, but for semiconductors with appreciable gaps, band gap underestimation usually has minor influence on transport coefficients because hole transport is essentially determined by structural features of VB and electron transport is determined by structural features of CB, gaps between them do not really matter. Anyway, in subsequent calculations of transport coefficients, we have shifted energies of CB to match experimental band gaps.

3.1.2 Seebeck coefficients. To calculate transport coefficients by the Boltzmann transport theory, band energies on a fine **k**-mesh, which is 21 × 21 × 11 for pentacene and 13 × 13 × 13 for rubrene, are generated since the transport distribution kernel of eqn (19) is a summation over **k**. Convergence test has been performed with a denser **k**-mesh. The band interpolation method proposed by Madsen and Singh[40,41] is used to obtain analytical expressions of band energies that allow for accurate determination of velocities from band energies. Calculations of transport coefficients are performed with the BoltzTraP program that is interfaced to the electronic structure package VASP.[42] To show anisotropic thermoelectric transport, the transport tensors of interest are output in three crystal directions.

The transport coefficients and charge carrier concentration both change with the Fermi level position, as such the transport coefficients can be obtained as a function of charge carrier concentration. Field-effect-modulated thermopower measurements have been realized on crystalline organic semiconductors.[30,43] In these measurements, the influence of a gate insulator on the Seebeck coefficient is not obvious, suggesting that the underlying mechanisms should represent intrinsic properties of organic semiconductors. We thereby compare the Seebeck coefficient measured in the field-effect transistor (FET) geometry with our calculations. In the FET structure, field-induced charge carriers move along the interface between the organic semiconductor and the dielectric gate, and conduction occurs on the surface of the semiconductor.[44] So we convert charge carrier concentration to charge carrier density on the surface of semiconductors by multiplying it with the thickness of the conduction channel, T_{int}. The value of T_{int} is taken as 15 Å for pentacene as done in the literature (ref. 45) and 27 Å for rubrene which corresponds to approximately two molecular layers. The calculated and measured Seebeck coefficients as a function of charge carrier density at room temperature are presented in Fig. 3. The FET measurements were on holes because only holes can be injected. Fig. 3 shows that the calculated Seebeck coefficient decreases

View Article Online

Published on 06 September 2012. Downloaded by Tsinghua University on 06/04/2014 04:02:06.

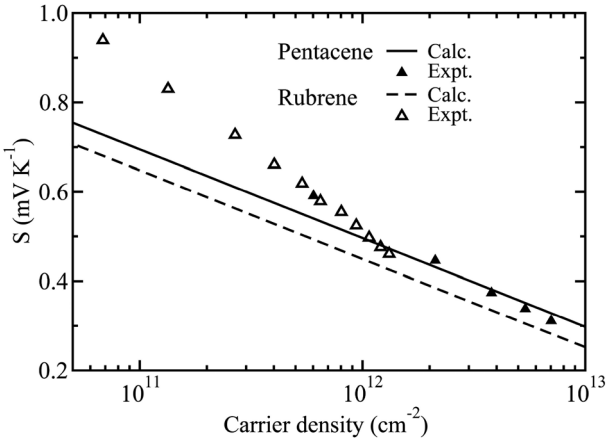

Fig. 3 Seebeck coefficients calculated for pentacene and rubrene at room temperature as a function of charge carrier density, in comparison with the FET measurements. Reprinted with permission from ref. 13. Copyright 2009 American Institute of Physics.

logarithmically with increasing carrier concentration, in reasonable agreement with the experimental observations.[30]

3.1.3 Anisotropic thermal transport. The lattice thermal conductivities of pentacene thin films and rubrene single crystals have been measured experimentally,[31,32] but the measurements were made largely in the direction perpendicular to the molecular packing plane. Actually in molecular crystals thermal transport is anisotropic as charge transport, and accurate modeling of phonon transport is important for prediction of anisotropic thermoelectirc performance in organic crystals. To study anisotropic thermal transport in pentacene, we perform nonequilibrium molecular dynamics simulations with the general amber force field (GAFF)[46] and the OPLS united-atom force field[47,48] and with the LAMMPS simulation package.[49] To assess the performance of the two force fields, we first apply them to predict phonon density of states and heat capacity of pentacene. Though heat capacity is underestimated compared to the experimental value,[50] both force fields give reasonable predictions.

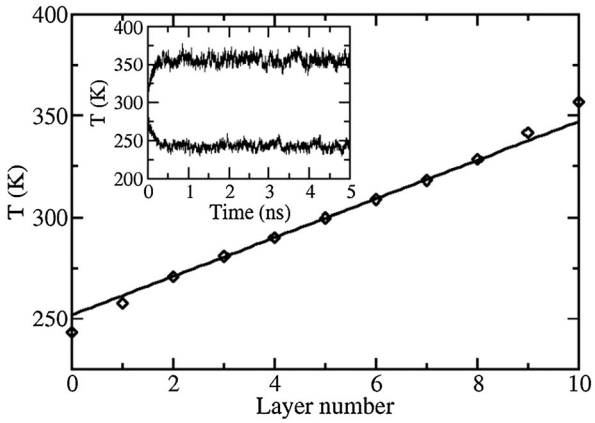

Fig. 4 Temperature profile along the **a** axis for box dimensions 40 × 3 × 2 obtained from nonequilibrium MD simulations. The solid line represents the linear fit of the data points. The inset shows the time evolution of temperature of heat sink and source. Reprinted with permission from ref. 14. Copyright 2011 American Chemical Society.

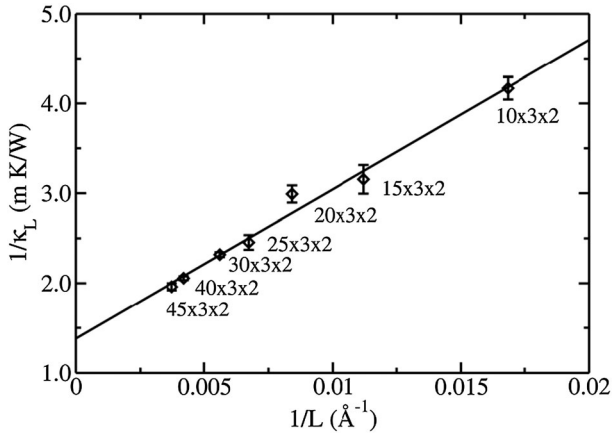

Fig. 5 Inverse of the lattice thermal conductivity *versus* inverse of the box length in the direction of **a**. Reprinted with permission from ref. 14. Copyright 2011 American Chemical Society.

In the nonequilibrium MD simulations, the simulation box is divided into 20 layers. The Müller-Plathe algorithm is applied to induce a heat current in the system. As an example, the temperature profile obtained is shown in Fig. 4. The profile is essentially linear, except for the region near the heat sink, layer 0, and the heat source, layer 10. The temperature dropoff at the heat sink and pickup at the heat source are caused by unphysical exchange of momentum between the two layers, which is not well balanced by physical heat flow. The temperature gradient is obtained by linear regression of the data points in the linear region of the profile. The heat current is calculated according to eqn (34), and finally the lattice thermal conductivity is extracted by Fourier's law.

To obtain the lattice thermal conductivity of a true bulk system, simulations at several box lengths are performed. The linear dependence of inverse of the lattice thermal conductivity on inverse of the box length is confirmed by the simulation data, as shown in Fig. 5. Linear extrapolation of the data gives the lattice thermal conductivity of 0.72 W m^{-1} K^{-1} in the direction of **a***. The effective phone mean free path can be derived from the extrapolation procedure as $l_{bulk} = v\tau_{bulk} = B/2A$, which yields a value of 60.3 Å in the direction of **a***. The lattice thermal conductivities in the other two crystal directions **b*** and **c*** are obtained similarly, and the values are 1.1 and 0.61 W m^{-1} K^{-1} respectively. The corresponding phonon mean free paths are 392.6 Å and 42.3 Å. The phonon transport in the pentacene crystal exhibits an anisotropy of **b*** > **a*** > **c***, which is in line with that found in the charge transport, except that an anisotropy of two is found for the former whereas an anisotropy of two orders of magnitude for the latter. In comparison with GAFF, OPLS united-atom force field tends to underestimate lattice thermal conductivities. With the united-atom force field, the degrees of freedom of the system are greatly reduced, and computer times are substantially saved, but for accurate prediction of lattice thermal conductivities, the all-atom force field has to be used.

The experimental measurements on pentacene thin films give a lattice thermal conductivity of 0.51 W m^{-1} K^{-1} in the direction perpendicular to the film plane.[31] Our calculations predict a lattice thermal conductivity of 0.61 W m^{-1} K^{-1} in the

 This journal is © the Owner Societies 2012

View Article Online

Published on 06 September 2012. Downloaded by Tsinghua University on 06/04/2014 04:02:06.

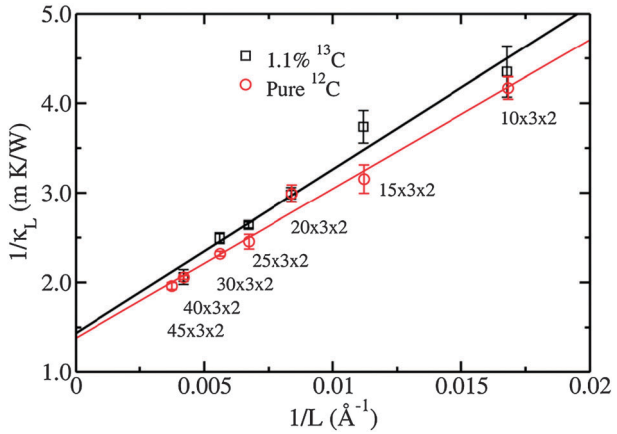

Fig. 6 Effects of isotopic substitution on the lattice thermal conductivity. Reprinted with permission from ref. 14. Copyright 2011 American Chemical Society.

direction of **c***, which agrees reasonably well with the experimental value. It should be noted that statistical errors associated with the simulations are ~5%, and extrapolation to the infinite-size limit tends to magnify the statistical errors. Meanwhile, our calculations are performed for a perfect crystal where phonon scatterings contribute exclusively to thermal transport. In real materials, phonons are also subject to defect and boundary scatterings, which leads to further reduction in phonon lifetimes and mean free paths, in turn further reduction in the lattice thermal conductivity.

In the following we consider two types of defects, namely isotopic substitutions and vacancies. The lattice thermal conductivity of pentacene containing 1.1% natural abundance of ^{13}C is calculated. The substitution sites of ^{13}C are chosen randomly. Simulations have been performed for box dimensions of 10, 15, 20, 25, 30, and 40 cells in the direction of **a**. Fig. 6 shows inverse of the lattice thermal conductivity *versus* inverse of the box length for 1.1% ^{13}C and pure ^{12}C pentacene. We find that the lattice thermal conductivity for pentacene with natural abundance of ^{13}C is always slightly lower than that for pure ^{12}C at a certain box length. The extrapolated lattice thermal conductivity for 1.1% ^{13}C is 0.70 W m^{-1} K^{-1}, in comparison with 0.72 W m^{-1} K^{-1} for pure ^{12}C. For diamond

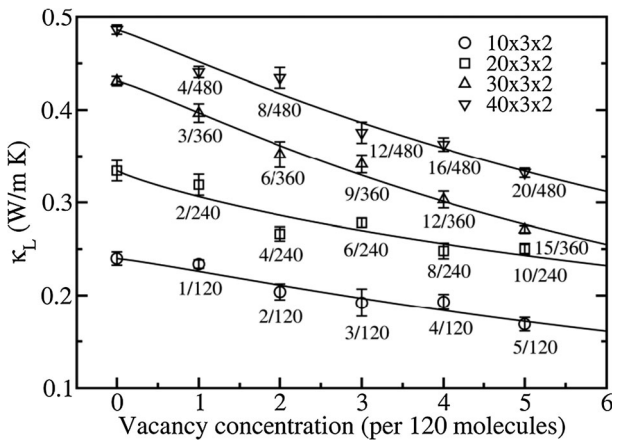

Fig. 7 Effects of vacancies on the lattice thermal conductivity. Reprinted with permission from ref. 14. Copyright 2011 American Chemical Society.

the ratio of lattice thermal conductivity for pure ^{12}C to that for 1.1% ^{13}C is 1.45 ± 0.16, which was obtained from equilibrium MD simulations.[21] It shows that phonon transport in pentacene is much less sensitive to the isotopic substitution than that in diamond.

The effects of vacancies on lattice thermal conductivities are also studied. The box dimensions of 10, 20, 30, and 40 cells respectively in the direction of **a** and a random distribution of vacancies are created. Fig. 7 shows that the lattice thermal conductivity at the fixed box length decreases rapidly with increasing vacancy concentration, n_v. Following the practice of ref 21, we fit results in Fig. 7 with

$$\kappa_{\mathrm{tot}}(n_v) = \frac{\kappa_{\mathrm{perf}}}{1 + C n_v{}^{\alpha}} \qquad (38)$$

and a scaling factor of 1.16, 0.94, 1.16, and 1.11 is obtained for the box length of 10, 20, 30, and 40 cells respectively. The fit in eqn (38) suggests that vacancy contribution to the lattice thermal conductivity obeys a scaling law of $\kappa_{\mathrm{vac}} \propto n_v{}^{-\alpha}$. The scaling factor for pentacene is found to be larger than that for diamond (~ 0.7),[21] which suggests that phonon transport in pentacene is more sensitive to vacancies than that in diamond.

3.1.4 Thermoelectric figure of merit. The Seebeck coefficient S, electrical conductivity σ, thermoelectric power factor $S^2\sigma$, electronic thermal conductivity κ_e, and dimensionless figure of merit $zT = S^2\sigma T/(\kappa_e + \kappa_L)$ at room temperature have been shown as a function of charge carrier concentration in Fig. 8. In the constant relaxation time approximation, only the absolute value of S is obtained since it is defined as the ratio of two transport coefficients, other transport coefficients are obtained with respect to τ. Fig. 8 shows that at low charge

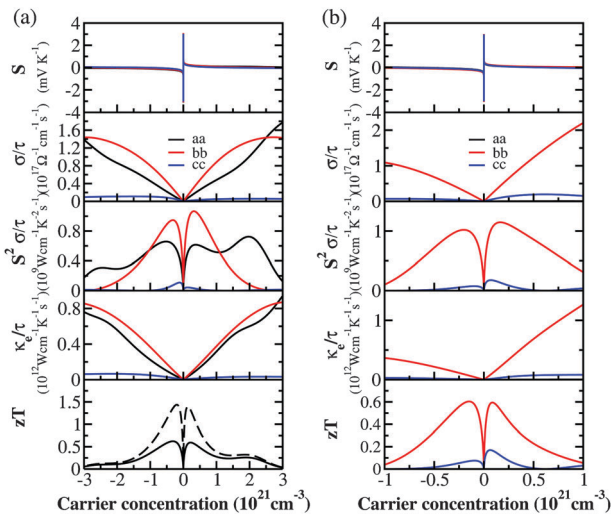

Fig. 8 Transport coefficients calculated for (a) pentacene and (b) rubrene at room temperature as a function of charge carrier concentration. The zT values of pentacene in the direction of **a** are evaluated based on the empirical relaxation times of 31 fs (solid line) and 97 fs (dashed line) respectively and the calculated lattice thermal conductivity of 0.72 W m^{-1} K^{-1}. The zT values of rubrene are estimated based on the empirical relaxation times of 12 fs in the direction of **b** and 17 fs in the direction of **c**, and the experimental lattice thermal conductivity of 0.5 W m^{-1} K^{-1}. Reprinted with permission from ref. 13. Copyright 2009 American Institute of Physics.

View Article Online

Published on 06 September 2012. Downloaded by Tsinghua University on 06/04/2014 04:02:06.

carrier concentration, the Seebeck coefficient is large whereas the electrical conductivity is low, and the opposite trend is seen at high charge carrier concentration. As a result, there exists an optimal doping level at which the value of zT is maximized. To evaluate zT, the relaxation time has to be supplied as a parameter. The charge carrier mobility with respect to τ can be obtained *via* the relation $\sigma = \mu eN$ from the calculated σ–N profiles. The relaxation time τ is then derived by fitting the calculated mobilities to the experimental values. The temperature dependence of hole mobilities in the ultrapure pentacene crystals has been extracted from the space charge-limited current measurements.[51] At room temperature, a mobility of 11.2 $cm^2\ V^{-1}\ s^{-1}$ is obtained assuming a uniform current distribution across the crystal whereas a mobility of 35 $cm^2\ V^{-1}\ s^{-1}$ is extracted assuming an anisotropy of conductivity factor of 10^2 along the **a** and **c** axes.[51] The relaxation time is then estimated to be 31 fs and 97 fs respectively by fitting the experimental hole mobilities to the calculated ones in the crystal direction of **a**. The zT value is evaluated based on the electrical transport coefficients and the lattice thermal conductivity both calculated in the **a** direction. It exhibits a peak value of 0.6 with charge carrier concentration of 2×10^{20} cm^{-3} for $\tau = 31$ fs, whereas a peak value of 1.4 is exhibited with carrier concentration of 1×10^{20} cm^{-3} for $\tau = 97$ fs. The temperature dependence of both charge and phonon transport in pentacene has been well characterized experimentally,[31,51] which allows us to evaluate the temperature dependence of thermoelectric properties.

We find that the thermoelectric figure of merit is enhanced at low temperatures.

The FET mobility of rubrene extracted from four-probe measurements of conductivity along the **b** and **c** axes is 20 and 8 $cm^2\ V^{-1}\ s^{-1}$, respectively, at room temperature.[52] By fitting the experimental and theoretical mobilities, a relaxation time of 12 fs and 17 fs is derived respectively along the **b** and **c** axes. The dimensionless figure of merit is estimated with the lattice thermal conductivity of 0.5 $W\ m^{-1}\ K^{-1}$. zT in the crystal direction of **b** exhibits a peak value of 0.6 at the carrier concentration of 8×10^{19} cm^{-3}. In contrast to pentacene, rubrene shows moderate thermoelectric figure of merit. The difference in zT between pentacene and rubrene is attributed mainly to the difference in the Seebeck coefficients of these materials at the optimal doping level. Excellent thermoelectric performance requires both large Seebeck coefficients and high charge carrier mobilities, which in turn require both flat and dispersed bands around the Fermi level. These distinctive band features have been observed in pentacene.

3.2 Phthalocyanine and metal phthalocyanines

Phthalocyanine (Pc) is a versatile class of organic semiconducting materials with interesting charge transport and optical properties. Literature reported that the Seebeck coefficients of phthalocyanines fall into the range of 0.6–1.8 $mV\ K^{-1}$,[53] and the charge carrier mobilities in single crystal Pcs by Hall measurement is on the order of $cm^2\ V^{-1}\ s^{-1}$.[54] The highest field-effect mobility of holes in thin films of TiOPc was reported to be 10 $cm^2\ V^{-1}\ s^{-1}$, in good agreement with our theoretical value.[55] The high charge carrier mobilities and the large Seebeck coefficients suggest that metal phthalocyanines could be potential thermoelectric materials. On the basis of the study of pentacene and rubrene in the constant relaxation time approximation, we push a step forward to study thermoelectric transport in phthalocyanine and metal phthalocyanines by calculating the relaxation time based on the deformation potential theory.[56] It should be pointed out that our computational scheme used to study Pcs is completely parameter free.

3.2.1 Band structures. Pc is a macrocyclic molecule that can host metal elements like Cu, Ni, and TiO in its central cavity. Metal phthalocyanines form various polymorphs in which the molecular stacking arrangements and alignment can be profoundly different. We target α-form H_2Pc, CuPc, NiPc, and TiOPc whose crystal structures are quite different, see Fig. 9. In particular, the crystal structure of TiOPc differs significantly from that of the other three Pcs. H_2Pc, CuPc, and NiPc are planar molecules, whereas TiOPc has a protruding titanyl group and adopts a nonplanar square pyramidal structure. There exist four, two, and one molecules respectively in the unit cell of H_2Pc, NiPc, and CuPc, and the closest molecular stacking is in the direction of **b**, **b**, and **a** with the lattice constant much shorter than that in other two directions. The crystal of TiOPc is triclinic with lattice constants comparable in three crystal directions. The unit cell of TiOPc contains two inequivalent molecules giving rise to two types of interactions, the so-called convex- and concave-type dimers.[57] The convex and concave interactions are determined by the relative orientations of the protruding titanyl groups. The convex interactions involve TiOPc molecules with the titanyl groups facing each other, while the concave interactions with the titanyl groups oriented on opposite sides of the molecules, see Fig. 9(d). As in the study of pentacene and rubrene, the PBE functional was used for electronic structure calculations. In atomic coordinates optimization, a Monkhorst–Pack **k**-mesh of $2 \times 12 \times 2$, $8 \times 2 \times 2$, $3 \times 12 \times 4$, and $6 \times 6 \times 9$ was used for H_2Pc, CuPc, NiPc, and TiOPc respectively. The calculated band structures and DOS of H_2Pc, CuPc, NiPc, and TiOPc are displayed in Fig. 10. Molecular stackings exhibit a critical influence on band structures. Since there are four, one, two, and two molecules in the unit cell of H_2Pc, CuPc, NiPc, and TiOPc, there exist four, one, two, and two subbands in the highest VB and lowest CB, which are highlighted in red. The splittings of subbands are small for H_2Pc and NiPc but notably large for TiOPc because the convex and concave interactions are quite different. In the case of CuPc and NiPc, the band width of CB is larger than that of VB, which

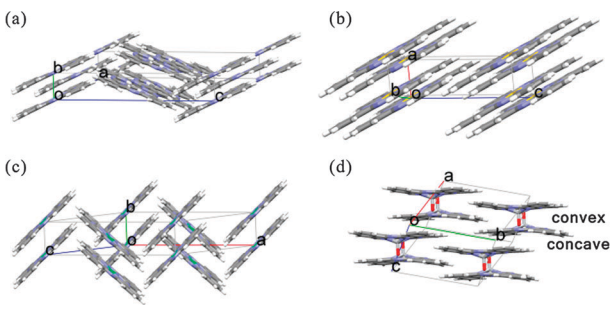

Fig. 9 Crystal structures of (a) H_2Pc, (b) CuPc, (c) NiPc, and (d) TiOPc. Reprinted with permission from ref. 56. Copyright 2012 American Chemical Society.

 This journal is © the Owner Societies 2012

View Article Online

Published on 06 September 2012. Downloaded by Tsinghua University on 06/04/2014 04:02:06.

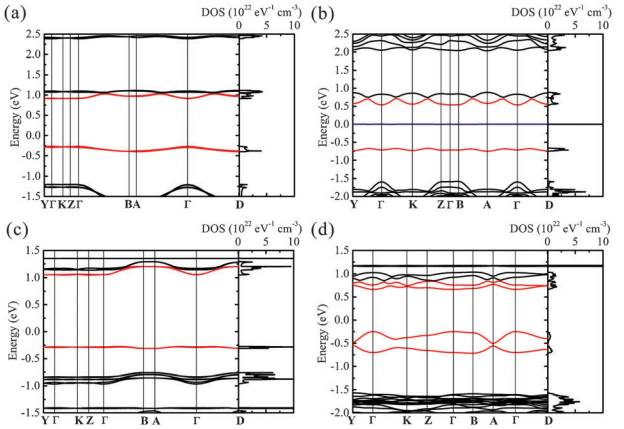

Fig. 10 Band structures and DOS of (a) H_2Pc, (b) CuPc, (c) NiPc, and (d) TiOPc. The reciprocal coordinates of high-symmetry points are Γ = (0, 0, 0), Y = (0.5, 0, 0), K = (0.5, 0, 0.5), B = (0, 0.5, 0), Z = (0, 0, 0.5), A = (0.5, 0.5, 0) and D = (0.5, 0.5, 0.5) respectively. Reprinted with permission from ref. 56. Copyright 2012 American Chemical Society.

indicates that electrons might move faster than holes. The small band width of VB in NiPc gives rise to a sharp DOS, which is a characteristic feature for a large Seebeck coefficient. In the case of TiOPc, the band width of VB is larger than that of CB.

The band gaps of H_2Pc, CuPc, NiPc and TiOPc are calculated to be 1.18, 1.25, 1.34 and 0.91 eV respectively. A localized state is observed in the band gap of CuPc. The single electron in this state is immobile so it has no contribution to charge transport. The trap state was ignored when we calculated electrical transport properties. CuPc is intrinsically a semiconductor even if it has an odd number of electrons. As shown before, band gaps were underestimated by DFT calculations, but the underestimation of band gaps should have minimal influence on charge transport, because it is band width, not band gap, that determines transport properties.

3.2.2 Relaxation times. In the constant relaxation time approximation, the relaxation time is often supplied as an empirical parameter, which can be estimated from experimental measurement of transport coefficients. The evaluation of relaxation time from first-principles is rarely done in thermoelectric studies. Indeed, characterization of electron–phonon interactions is the most challenging task in transport theory. When the electron–phonon coupling is weaker than the intermolecular electronic coupling, phonon scattering effect on electrons can be treated as perturbation. We show first-principles calculations of relaxation times by the deformation potential theory in the long wavelength limit.

To consider anisotropic scattering effects, we dilate the lattice in three crystal directions **a**, **b**, and **c** respectively, and calculate the deformation potential constant E_1 and elastic constant C_{ii} in three spatial directions. The scattering matrix element $|M(\mathbf{k},\mathbf{k}')|^2$ of electrons by acoustic phonons propagating in the direction of **a**, **b**, and **c** were computed individually and the average value was used in eqn (31).

To obtain the deformation potential constant E_1 in each direction, we deformed the lattice in that direction and calculated band energies in the deformed lattice. The displacement of the bottom of CB upon dilation was used to evaluate the deformation potential constant for electrons, the displacement of the top of VB was used to evaluate the deformation potential constant for holes. The deformation potential constant was defined as $E_1 = \Delta\varepsilon/(\Delta l/l_0)$, where $\Delta\varepsilon$ is the band edge shift due to lattice dilation $\Delta l/l_0$. When not-so-heavily doped, only subbands near the band edge of CB and VB contribute to charge transport. It is noted that band edge is usually more sensitive to the lattice deformation than other subbands, so band edge shift usually gives an upper limit of the deformation potential constant for other subbands. Besides, we assumed that the lowest energy band was not influenced by dilation, so it was taken as reference when the band edge shift of CB and VB was evaluated. The deformation potential constants for electrons and holes in three crystal directions were summarized in Table 1. It shows that the deformation potential constants are indeed anisotropic, due to the anisotropic molecular packings in organic molecular crystals.

Table 1 Deformation potential constants in eV for both electrons and holes in Pcs

	E_1^a (h)	E_1^b (h)	E_1^c (h)	E_1^a (e)	E_1^b (e)	E_1^c (e)
H_2Pc	0.60	1.72	0.93	0.35	0.93	2.03
CuPc	0.31	0.31	0.36	0.26	0.23	1.24
NiPc	0.72	0.03	0.53	0.40	0.69	0.35
TiOPc	1.75	0.59	1.49	0.02	0.36	0.71

The elastic constants were obtained by fitting the total energy of the deformed lattice to dilation through the relation $\Delta E/V_0 = C_{ii}(\Delta l/l_0)^2/2$, where ΔE is the total energy change due to the dilation $\Delta l/l_0$. The calculated elastic constants of Pcs were provided in Table 2. The elastic constants are less anisotropic than the deformation potential constants, and the magnitude of elastic constants for Pcs is close to each other. With the deformation potential constant and elastic constant, we calculated the relaxation time using eqn (31). In the calculation of relaxation time and transport coefficients, band energies on a fine **k**-mesh of 5 × 31 × 5, 35 × 9 × 9, 7 × 25 × 9, and 9 × 9 × 11 were obtained for H_2Pc, CuPc, NiPc, and TiOPc respectively, and interpolated onto a **k**-mesh ten times as dense as the original one. Since both the deformation potential constant and elastic constant are anisotropic, the

Table 2 Elastic constants of Pcs in 10^9 J m^{-3}

	C_{ii}^a	C_{ii}^b	C_{ii}^c
H_2Pc	12.1	8.2	15.9
CuPc	7.8	12.0	11.4
NiPc	11.5	13.2	11.9
TiOPc	13.8	14.0	10.1

Table 3 Relaxation times in fs averaged over the highest VB and lowest CB

	τ (h)	τ (e)
H_2Pc	50.4	49.5
CuPc	118.7	60.9
NiPc	48.4	231.5
TiOPc	50.6	188.6

View Article Online

Published on 06 September 2012. Downloaded by Tsinghua University on 06/04/2014 04:02:06.

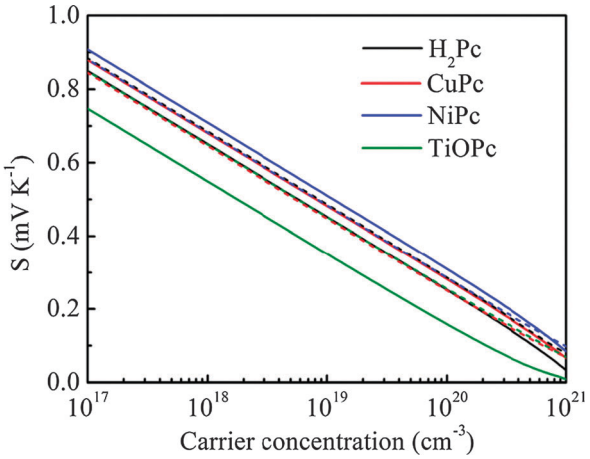

Fig. 11 Seebeck coefficients as a function of logarithm of charge carrier concentration. The Seebeck coefficients of holes are represented by solid lines and those of electrons by dashed lines. Reprinted with permission from ref. 56. Copyright 2012 American Chemical Society.

scattering matrix elements are anisotropic. The scattering matrix element averaged over **a**, **b**, and **c** directions was used for calculation of the relaxation time. The average relaxation times of Pcs for electrons in the lowest CB and holes in the highest VB were collected in Table 3. The magnitude of relaxation times range from several tens of fs to several hundreds of fs.

3.2.3 Seebeck coefficients and thermoelectric power factor. The original BoltzTraP program was designed for use in the constant relaxation time approximation. We implemented the relaxation time calculation in the program and obtained the absolute values of transport coefficients of interest at the temperature of 298 K. It is found that the Seebeck coefficient decreases linearly with the Fermi level, and the carrier concentration increases exponentially with the Fermi level. The Seebeck coefficients of Pcs were displayed in Fig. 11 as a function of logarithm of charge carrier concentration. A linear relationship showed up as we have seen in the case of pentacene and rubrene. The Seebeck coefficients of phthalocyanine crystals were measured early in the 1960s.[53] The α-form H_2Pc, CuPc, and NiPc crystals were reported to possess a Seebeck coefficient of 1.25, 0.91, and 0.97 mV K^{-1}, respectively at 300 K. The maximum Seebeck coefficients of H_2Pc, CuPc, NiPc, and TiOPc were 1.85, 1.86, 1.49 and 1.38 mV K^{-1} calculated for holes, and -1.52, -1.52, -2.19 and -1.47 mV K^{-1} for electrons, which was in reasonable agreement with the experimental values. The electron Seebeck coefficient of NiPc was the largest in magnitude among the Pcs, which was in accord with our early judgement based on observation of a sharp DOS near the band edge. The hole Seebeck of TiOPc was the smallest, which corresponded to a smooth DOS near the band edge. Overall, difference in the maximum Seebeck coefficients was not appreciably large among the phthalocyanine crystals, nor was it between electrons and holes.

The electrical conductivity increases with increasing carrier concentration whereas the Seebeck coefficient decreases with increasing carrier concentration, consequently the thermoelectric power factor shows a peak value. These features show

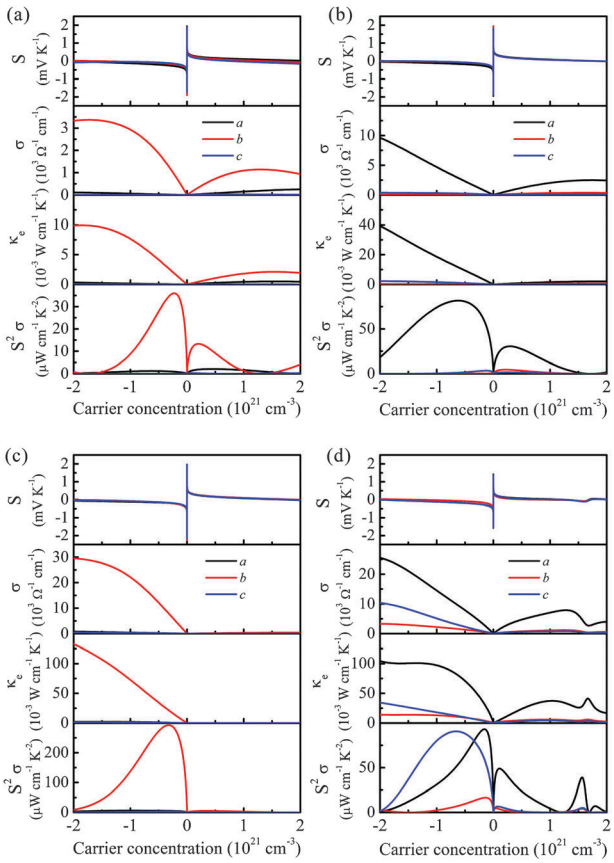

Fig. 12 Electrical transport coefficients calculated for (a) H_2Pc, (b) CuPc, (c) NiPc, and (d) TiOPc. Reprinted with permission from ref. 56. Copyright 2012 American Chemical Society.

that accurate doping can be one of effective ways to control the thermoelectric performance of a material. Controlled p-doping of phthalocyanines by strong electron acceptors was investigated by combined Seebeck and conductivity measurements.[58,59] A novel n-type doping technique by strong donors was developed to enable the n-type conduction in metal phthalocyanines.[60] The transport coefficients were displayed in Fig. 12 as a function of carrier concentration. It shows that the power factors of n-doped phthalocyanines are higher than those of p-doped, suggesting that all phthalocyanine crystals studied are n-type thermoelectric materials. The maximum power factors of H_2Pc, CuPc, NiPc, and TiOPc were 36.0, 81.7, 292.8, and 93.1 W cm^{-1} K^{-2}, respectively when n-doped. The optimal doping levels predicted on the basis of first-principles calculations can provide useful guidance to control experimental conditions in order to achieve the best thermoelectric performance of a material.

3.2.4 Best thermoelectric performance. To fully characterize a thermoelectric material, accurate modeling of phonon transport is necessary. We have shown for pentacene that nonequilibrium MD approach with the GAFF can give a reliable prediction of the lattice thermal conductivity. It has been noticed that the thermoelectric performance of molecular crystals is profoundly anisotropic, and the largest power factor is found in the crystal direction of **b**, **a**, **b**, and **a** for H_2Pc, CuPc, NiPc, and TiOPc respectively. The best thermoelectric performance is actually

 This journal is © the Owner Societies 2012

View Article Online

Published on 06 September 2012. Downloaded by Tsinghua University on 06/04/2014 04:02:06.

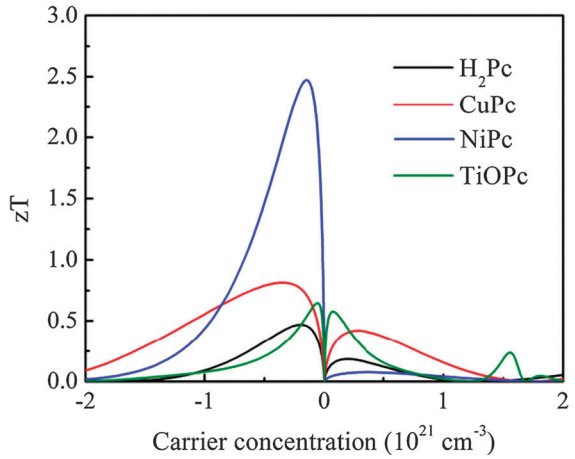

Fig. 13 Dimensionless figure of merit estimated for H2Pc, CuPc, NiPc, and TiOPc in the direction of **b**, **a**, **b**, and **a** respectively. The lattice thermal conductivity of 2.1 W m^{-1} K^{-1}, calculated in the direction of **b** for H_2Pc was used in the estimation. Reprinted with permission from ref. 56. Copyright 2012 American Chemical Society.

found in the direction in which the crystal shows the closest molecular packing, and in that direction the lattice thermal conductivity is the largest. Since we are only interested in thermoelectric transport in these directions, we calculate the lattice thermal conductivity of H_2Pc in the direction of **b***. The value is 2.1 W m^{-1} K^{-1} from nonequilibrium MD simulations with the GAFF. We notice that the lattice constant of three metal phthalocyanines in the direction of closest packing is comparable to or larger than that of H_2Pc, so we take the lattice thermal conductivity of H_2Pc as an upper limit of that of other Pcs, and use it in the evaluation of zT in the direction of best thermoelectric performance. The dimensionless figure of merit at 298 K *versus* carrier concentration is shown in Fig. 13. As we have seen in power factors, all Pcs can reach a maximum zT whether n-doped or p-doped, but apparently the dimensionless figure of merit is higher when n-doped. Along the **b** axis, the zT value of H_2Pc can reach 0.5 with a doping level of -2.0×10^{20} cm^{-3}, in the case of CuPc, along the **a** axis zT can reach 0.8 with a doping level of -3.5×10^{20} cm^{-3}. The zT value of NiPc shows a peak value of 2.5 at a carrier concentration of -1.5×10^{20} cm^{-3}, and that of TiOPc has a peak value of 0.6 at a carrier concentration of -1.0×10^{20} cm^{-3}. NiPc is the best n-type thermoelectric material among all the Pcs we studied, which is in line with the observation that NiPc has the largest electron Seebeck coefficient among the Pcs.

4 Thermoelectric transport in conducting polymers

Conducting polymers such as polyacetylene, polypyrroles, polyanilines, polythiophenes, and polycarbazoles, as potential thermoelectric materials have attracted great attention and intensive experimental investigation, see a recent review[8] and references therein. Optimization of the thermoelectirc figure of merit has been shown by the accurate control of the doping level, and a zT value of 0.25 at room temperature was recently reported for poly(3,4-ethylenedioxythiophene) (PEDOT) nanowires.[9] As a final application of the theories introduced, we investigate thermoelectric transport in a single poly-(3-hexylthiophene) (P3HT) chain. The repeating unit of a one-dimensional (1D) P3HT chain is shown in Fig. 14 The lattice constant in the chain direction **b** and atomic coordinates are optimized by the PAW method with the local density approximation (LDA) on a $1 \times 4 \times 1$ **k**-mesh. The unit cell lengths in the in-plane **a** and out-of-plane **c** directions are fixed at 40 Å and 20 Å respectively, which are large enough to avoid inter-chain interactions. The optimized b parameter is 7.74 Å, in good agreement with the experimental values of 7.66 and 7.75 Å. The preference of LDA over GGA functional is based on our experiences that LDA optimization of the lattice constants for molecular crystals usually provides a better agreement with the experimental values than GGA functionals. Actually for covalently bonded molecular chains, differences arising from functionals are insignificant, as found in our early study of single-layer graphene sheet.[61] We also found that for double-layer graphene sheet where noncovalent interactions exist, LDA optimized inter-layer distance was in excellent agreement with the experimental value, and it even performed better than PBE-D functional with dispersion correction.[61] The band structures and DOS of P3HT are displayed in Fig. 15. The band widths of CB and VB are 1.54 eV and 2.03 eV respectively. The band gap is 1.04 eV at the Γ-point. For 1D system, DOS is converted to the linear density *via* multiplying the cross-sectional area by the volumetric density. The bottom of CB and the top of VB are relatively flat, giving rise to sharp DOS distributions at the band edges.

To calculate the deformation potential constant and elastic constant, the lattice is deformed in the direction of **b** with dilation of 0.5%, 1%, 1.5%, and 2% minus and plus respectively. The elastic constant is obtained by a parabolic fit of the total energy to the dilation, as shown in Fig. 16 (a), which gives a value of 10.1×10^9 J m^{-3}. The linear fit of the band edge shift to the dilation, shown in Fig. 16 (b) yields the deformation potential constant of 9.69 eV for electrons and

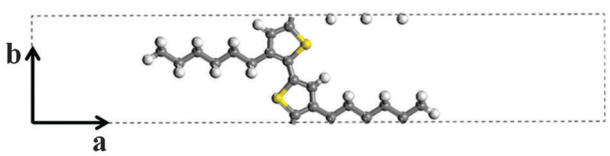

Fig. 14 The repeating unit of P3HT chain.

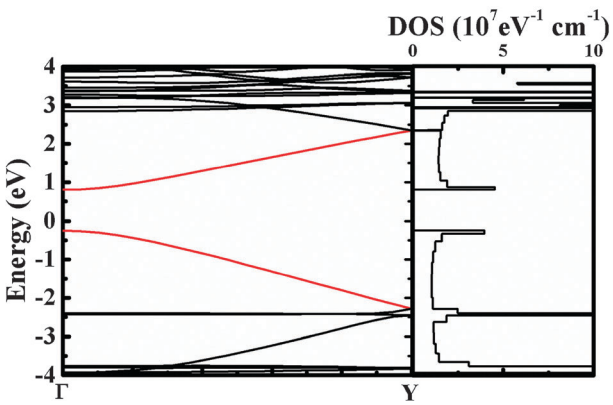

Fig. 15 Band energies and DOS of single P3HT chain.

View Article Online

Published on 06 September 2012. Downloaded by Tsinghua University on 06/04/2014 04:02:06.

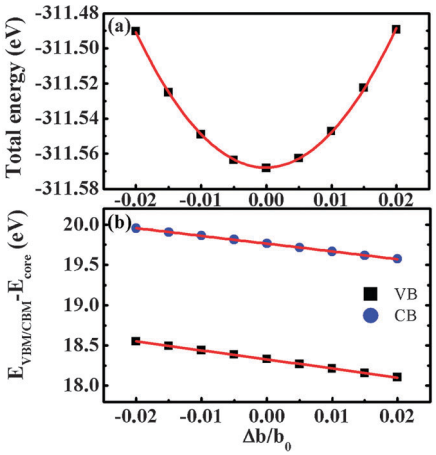

Fig. 16 (a) Total energy and (b) band edge shift upon lattice dilation.

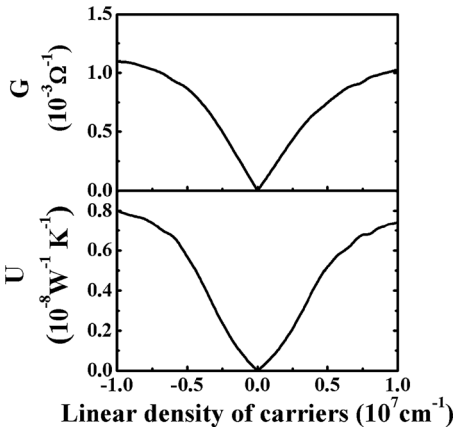

Fig. 17 Electrical conductance G and thermal conductance U calculated for P3HT as a function of linear density of carriers.

11.3 eV for holes. The transport coefficients are calculated on a $2 \times 800 \times 2$ **k**-mesh. For the 1D system, conductance instead of conductivity must be used. The electrical and thermal conductance at 298 K are displayed in Fig. 17 as a function of linear density of carriers. The Lorentz number, defined as $L = \kappa_e/(\sigma T)$, is found to be smaller than $(\pi^2/3)(k_B/e)^2$, violating the Wiedemann–Franz law.

To compare the thermoelectric performance of the single polymer chain to other systems, we use the crystal lattice parameters of P3HT, $a = 33.26$ Å and $c = 7.77$ Å, to define the cross-sectional area. The electrical and thermal conductivities are obtained, and shown in Fig. 18 as a function of linear density of carriers. The peak value of power factors is 1.7×10^{-5} W cm^{-1} K^{-2} for electrons, slightly higher than that for holes, which is 1.4×10^{-5} W cm^{-1} K^{-2}. It is noted that thermoelectric properties of single molecular chains of P3HT and PEDOT have been studied by Yang and co-authors with the small-polaron model.[62] The model relies on a variety of physical parameters, including intersite coupling, electron–phonon interaction, dielectric constant, chemical potential, and temperature. Only thermoelectric properties for the optical phonon induced polarons were considered. It is surprising to see that power factors predicted based on our band model do not differ much from those obtained by

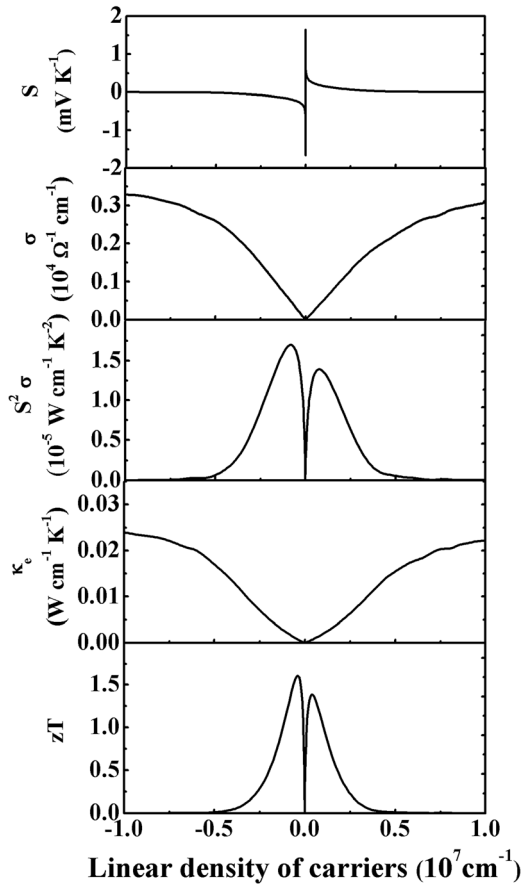

Fig. 18 Electrical transport coefficients calculated for a single P3HT chain as a function of linear density of carriers. The dimensionless figure of merit was estimated with the lattice thermal conductivity of 0.2 W m^{-1} K^{-1}.

Holstein's small-polaron model, considering that these two models and parameters adopted are profoundly different. For most polymer materials, phonon contribution to the thermal conductivity falls in the range of 0.1–1.0 W m^{-1} K^{-1} for bulk materials. As in ref. 62, we take the lattice thermal conductivity to be 0.2 W m^{-1} K^{-1} and estimate the dimensionless figure of merit of P3HT. When it is p-doped, the peak value of zT is 1.6 with the doping level of 4×10^5 cm^{-1}, and when it is n-doped the peak value of zT is 1.4 with the doping level of -4×10^5 cm^{-1}.

5 Conclusions and outlook

To conclude, we have developed a parameter free computational scheme to characterize thermoelectric figure of merit of organic materials including closely packed molecular crystals and single polymer chains. The phonon transport is modeled using the nonequilibrium MD approach with appropriate atomistic force fields that describe phonon–phonon interactions. The modeling of charge transport is based on the delocalized single electron picture. The electron is assumed to move in the periodic potential of the crystal lattice and the effective potential of other electrons. In the movement the electron is scattered by lattice waves, which in the long wavelength limit can be modeled by the deformation potential theory.

 This journal is © the Owner Societies 2012

View Article Online

Published on 06 September 2012. Downloaded by Tsinghua University on 06/04/2014 04:02:06.

With these approximations, the band-like description of charge transport requires no empirical parameters. All the electrical transport coefficients can be derived from first-principles electronic structure calculations. We have applied the theories and computation schemes to study thermoelectric transport in model systems such as molecular crystals with high charge carrier mobilities and one-dimensional polymer chains. The doping effect on the optimization of thermoelectric performance is focused upon. In particular, it is interesting to relate structural features of CB and VB to transport coefficients directly. In these studies, we have found that large band widths and sharp DOS are usually characteristic features of high thermoelectric power factors, which has been confirmed by calculations of transport coefficients.

It should be noted that theories that can be used to describe charge transport in organic materials have been debated for a long time. If the electronic coupling is larger than the electron–phonon coupling, a band-like model is appropriate in which charge carriers are in extended electronic states and scatterings by phonons are treated as perturbations. If the electron–phonon coupling is much larger than the electronic coupling, charge carriers can be entirely localized on one site, and a hopping model that describes charge transport as electron transfer between neighboring sites is recommended. So the charge transport mechanism in organic materials is really dependent on molecular structures, inter-molecular packings, and temperature. For closely-packed conjugated molecular crystals, a band picture often shows up in the low temperature regimes, and a hopping picture in the high temperature regimes. The band and hopping descriptions of charge transport are two limiting cases. Our modeling of thermoelectric transport is based on the band picture and provided predictions only in the band limit. The hopping model is based on two molecular parameters, namely inter-molecular transfer integral that characterizes the electronic coupling and intramolecular reorganization energy that characterizes the electron-vibrational coupling. The hopping model is simple yet has been proved useful in the design of materials with high charge carrier mobilities.[63] It is therefore of great interest to develop hopping models for study of thermoelectric transport in organic materials. We have never seen such kind of work to the best of our knowledge.

In between the band and hopping limits there exists the polaron model, which views charge transport as polaron transport. The polarons are also known as phonon-dressed charge carriers. Hannewald and co-authors have derived based on the Holstein Hamiltonian a general mobility expression that covers the whole temperature range, from the Boltzmann equation for band transport, through Holstein's small-polaron theory, to Marcus' electron transfer theory.[64] Thermoelectric transport coefficients of Holstein's small polaron model have been derived early in the 1960s using the Kubo formula.[65] Recently, Yang and co-authors investigated thermoelectric properties of qausi-one-dimensional molecular nanowires using Holstein's small polaron model.[62] The model relies on a few physical parameters such as inter-site coupling and electron–phonon interaction, which have to be derived by first-principles or empirically.

For the purpose of material design, a quantitative prediction of electrical transport coefficients is required. A challenging task is to characterize electron–phonon interactions at the first-principles level irrespective of which transport model is applied. A remarkable progress has been made in the density functional perturbation theory (DFPT)[66] within the framework of density functional theory. DFPT treats phonons as perturbations to the self-consistent potential produced by electrons and the nucleus. However, taking into account all phonon branches and phonon dispersions is still not computationally affordable. So far we have only seen applications of DFPT to simple systems such as graphene sheets for the calculation of electron–phonon couplings. Recently, a computational scheme taking advantage of the localized Wannier functions for both electrons and lattice vibrations was proposed,[67] and was applied to potassium-doped picene.[68] We also noticed that a charge patching method has been developed to calculate the electronic states for systems with tens of thousands atoms.[69] The method was used to calculate the electron–phonon couplings of disordered polythiophene bulk materials.[70] These advances will promote the fundamental understanding of charge transport in organic materials, and make modeling organic thermoelectric materials at the first-principles level possible.

Acknowledgements

This work is supported by the National Science Foundation of China (Grant Nos. 20920102031, 20903060, 21273124) and the Ministry of Science and Technology of China (Grant Nos. 2009CB623600, 2011CB932304, 2011CB808405). Computational resources are provided by the Supercomputing Center of the Chinese Academy of Sciences.

Notes and references

1 G. S. Nolas, J. Sharp and H. J. Goldsmid, *Thermoelectrics: Basic Principles and New Materials Developments*, Springer, Berlin; New York, 2001.
2 G. J. Snyder and T. S. Ursell, *Phys. Rev. Lett.*, 2003, **91**, 148301.
3 B. Sherman, R. R. Heikes and R. W. Ure, *J. Appl. Phys.*, 1960, **31**, 1–16.
4 M. S. Dresselhaus, G. Chen, M. Y. Tang, R. G. Yang, H. Lee, D. Z. Wang, Z. F. Ren, J. P. Fleurial and P. Gogna, *Adv. Mater.*, 2007, **19**, 1043–1053.
5 G. J. Snyder and E. S. Toberer, *Nat. Mater.*, 2008, **7**, 105–114.
6 M. Zebarjadi, K. Esfarjani, M. S. Dresselhaus, Z. F. Ren and G. Chen, *Energy. Environ. Sci.*, 2012, **5**, 5147–5162.
7 A. J. Minnich, M. S. Dresselhaus, Z. F. Ren and G. Chen, *Energy. Environ. Sci.*, 2009, **2**, 466–479.
8 N. Dubey and M. Leclerc, *J. Polym. Sci., Part B: Polym. Phys.*, 2011, **49**, 467–475.
9 O. Bubnova, Z. U. Khan, A. Malti, S. Braun, M. Fahlman, M. Berggren and X. Crispin, *Nat. Mater.*, 2011, **10**, 429–433.
10 D. K. Taggart, Y. A. Yang, S. C. Kung, T. M. McIntire and R. M. Penner, *Nano Lett.*, 2011, **11**, 125–131.
11 K. Hayashi, T. Shinano, Y. Miyazaki and T. Kajitani, *J. Appl. Phys.*, 2011, **109**, 023712.
12 K. Harada, M. Sumino, C. Adachi, S. Tanaka and K. Miyazaki, *Appl. Phys. Lett.*, 2010, **96**, 253304.
13 D. Wang, L. Tang, M. Q. Long and Z. G. Shuai, *J. Chem. Phys.*, 2009, **131**, 224704.
14 D. Wang, L. Tang, M. Q. Long and Z. G. Shuai, *J. Phys. Chem. C*, 2011, **115**, 5940–5946.
15 B. R. Nag, *Electron Transport in Compound Semiconductors*, Springer-Verlag, Berlin, New York, 1980.
16 T. J. Scheidemantel, C. Ambrosch-Draxl, T. Thonhauser, J. V. Badding and J. O. Sofo, *Phys. Rev. B*, 2003, **68**, 125210.

View Article Online

Published on 06 September 2012. Downloaded by Tsinghua University on 06/04/2014 04:02:06.

17 J. Bardeen and W. Shockley, *Phys. Rev.*, 1950, **80**, 72.
18 L. Tang, M. Q. Long, D. Wang and Z. G. Shuai, *Sci. China, Ser. B: Chem.*, 2009, **52**, 1646–1652.
19 G. P. Srivastava, *The Physics of Phonons*, Adam Hilger, Bristol, 1990.
20 S. G. Volz and G. Chen, *Phys. Rev. B: Condens. Matter Mater. Phys.*, 2000, **61**, 2651–2656.
21 J. W. Che, T. Cagin, W. Q. Deng and W. A. Goddard, *J. Chem. Phys.*, 2000, **113**, 6888–6900.
22 P. K. Schelling, S. R. Phillpot and P. Keblinski, *Phys. Rev. B: Condens. Matter Mater. Phys.*, 2002, **65**, 144306.
23 X. W. Zhou, S. Aubry, R. E. Jones, A. Greenstein and P. K. Schelling, *Phys. Rev. B: Condens. Matter Mater. Phys.*, 2009, **79**, 115201.
24 R. Kubo, M. Toda and N. Hashitsume, *Statistical Physics II*, Springer, Berlin, 1985.
25 P. Jund and R. Jullien, *Phys. Rev. B: Condens. Matter Mater. Phys.*, 1999, **59**, 13707–13711.
26 T. Ikeshoji and B. Hafskjold, *Mol. Phys.*, 1994, **81**, 251–261.
27 F. Müller-Plathe and D. Reith, *Comput. Theor. Polym. Sci.*, 1999, **9**, 203–209.
28 F. MullerPlathe, *J. Chem. Phys.*, 1997, **106**, 6082–6085.
29 H. Jiang, E. M. Myshakin, K. D. Jordan and R. P. Warzinski, *J. Phys. Chem. B*, 2008, **112**, 10207–10216.
30 K. P. Pernstich, B. Rossner and B. Batlogg, *Nat. Mater.*, 2008, **7**, 321–325.
31 N. Kim, B. Domercq, S. Yoo, A. Christensen, B. Kippelen and S. Graham, *Appl. Phys. Lett.*, 2005, **87**, 241908.
32 Y. Okada, M. Uno and J. Takeya, *Mater. Res. Soc. Symp. Proc.*, 2009, **1154**, B10–B59.
33 S. Schiefer, M. Huth, A. Dobrinevski and B. Nickel, *J. Am. Chem. Soc.*, 2007, **129**, 10316–10317.
34 O. D. Jurchescu, A. Meetsma and T. T. Palstra, *Acta. Crystallogr., Sec. B: Struct. Sci.*, 2006, **62**, 330–334.
35 P. E. Blochl, *Phys. Rev. B: Condens. Matter Mater. Phys.*, 1994, **50**, 17953–17979.
36 G. Kresse and D. Joubert, *Phys. Rev. B: Condens. Matter Mater. Phys.*, 1999, **59**, 1758–1775.
37 J. P. Perdew, K. Burke and M. Ernzerhof, *Phys. Rev. Lett.*, 1996, **77**, 3865–3868.
38 G. Kresse and J. Furthmuller, *Phys. Rev. B: Condens. Matter Mater. Phys.*, 1996, **54**, 11169–11186.
39 H. J. Monkhorst and J. D. Pack, *Phys. Rev. B: Solid State*, 1976, **13**, 5188–5192.
40 G. K. Madsen, *J. Am. Chem. Soc.*, 2006, **128**, 12140–12146.
41 G. K. H. Madsen and D. J. Singh, *Comput. Phys. Commun.*, 2006, **175**, 67–71.
42 J. Yang, H. M. Li, T. Wu, W. Q. Zhang, L. D. Chen and J. H. Yang, *Adv. Funct. Mater.*, 2008, **18**, 2880–2888.
43 A. von Muhlenen, N. Errien, M. Schaer, M. N. Bussac and L. Zuppiroli, *Phys. Rev. B*, 2007, **75**, 115338.
44 M. E. Gershenson, V. Podzorov and A. F. Morpurgo, *Rev. Mod. Phys.*, 2006, **78**, 973–989.
45 D. Oberhoff, K. P. Pernstich, D. J. Gundlach and B. Batlogg, *IEEE T. Electron Dev.*, 2007, **54**, 17–25.
46 J. M. Wang, R. M. Wolf, J. W. Caldwell, P. A. Kollman and D. A. Case, *J. Comput. Chem.*, 2004, **25**, 1157–1174.
47 W. L. Jorgensen, J. D. Madura and C. J. Swenson, *J. Am. Chem. Soc.*, 1984, **106**, 6638–6646.
48 W. L. Jorgensen and J. Tirado-Rives, *Proc. Natl. Acad. Sci. U. S. A.*, 2005, **102**, 6665–6670.
49 S. Plimpton, *J. Comput. Phys.*, 1995, **117**, 1–19.
50 M. Fulem, V. Lastovka, M. Straka, K. Ruzicka and J. M. Shaw, *J. Chem. Eng. Data*, 2008, **53**, 2175–2181.
51 O. D. Jurchescu, J. Baas and T. T. M. Palstra, *Appl. Phys. Lett.*, 2004, **84**, 3061–3063.
52 V. Podzorov, E. Menard, A. Borissov, V. Kiryukhin, J. A. Rogers and M. E. Gershenson, *Phys. Rev. Lett.*, 2004, **93**, 086602.
53 C. Hamann and I. Storbeck, *Naturwissenschaften*, 1963, **50**, 327.
54 G. H. Heilmeier and S. E. Harrison, *Phys. Rev.*, 1963, **132**, 2010–2016.
55 L. Q. Li, Q. X. Tang, H. X. Li, X. D. Yang, W. P. Hu, Y. B. Song, Z. G. Shuai, W. Xu, Y. Q. Liu and D. B. Zhu, *Adv. Mater.*, 2007, **19**, 2613–2617.
56 J. M. Chen, D. Wang and Z. G. Shuai, *J. Chem. Theory Comput.*, 2012, **8**, 3338–3347.
57 J. E. Norton and J. Brédas, *J. Chem. Phys.*, 2008, **128**, 034701.
58 M. Pfeiffer, A. Beyer, T. Fritz and K. Leo, *Appl. Phys. Lett.*, 1998, **73**, 3202.
59 M. Pfeiffer, T. Fritz, J. Blochwitz, A. Nollau, B. Plönnigs, A. Beyer and K. Leo, in: *Advances in Solid State Physics*, ed. B. Kramer, Springer Berlin/HeidelbergGermany, 1999, vol. 39, pp. 77–90.
60 K. Harada, A. G. Werner, M. Pfeiffer, C. J. Bloom, C. M. Elliott and K. Leo, *Proc. SPIE*, 2004, **5464**, 1–9.
61 J. Y. Xi, M. Q. Long, L. Tang, D. Wang and Z. G. Shuai, *Nanoscale*, 2012, **4**, 4348–4369.
62 Y. Y. Wang, J. Zhou and R. G. Yang, *J. Phys. Chem. C*, 2011, **115**, 24418–24428.
63 Z. G. Shuai, L. J. Wang and Q. K. Li, *Adv. Mater.*, 2011, **23**, 1145–1153.
64 F. Ortmann, F. Bechstedt and K. Hannewald, *Phys. Rev. B: Condens. Matter Mater. Phys.*, 2009, **79**, 235206.
65 K. D. Schotte, *Z. Phys.*, 1966, **196**, 393–414.
66 S. Baroni, S. de Gironcoli, A. Dal Corso and P. Giannozzi, *Rev. Mod. Phys.*, 2001, **73**, 515–562.
67 F. Giustino, M. L. Cohen and S. G. Louie, *Phys. Rev. B: Condens. Matter Mater. Phys.*, 2007, **76**, 165108.
68 M. Casula, M. Calandra, G. Profeta and F. Mauri, *Phys. Rev. Lett.*, 2011, **107**, 137006.
69 N. Vukmirovic and L. W. Wang, *J. Chem. Phys.*, 2008, **128**, 121102.
70 N. Vukmirovic and L. W. Wang, *Nano Lett.*, 2009, **9**, 3996–4000.

 This journal is © the Owner Societies 2012